

8. SITE 1227¹

Shipboard Scientific Party²

BACKGROUND AND OBJECTIVES

Site 1227 was one of three Leg 201 sites selected for drilling on the continental shelf of Peru. These shelf sites were collectively selected to provide records of microbial activities, communities, and geochemical consequences in organic-rich ocean-margin sediments.

The principal objectives at this site were

1. To test by comparison with other sites drilled during this expedition whether microbial communities, microbial activities, and the nature of microbe-environment interactions are different in organic-rich ocean-margin sediments than in open-ocean sediments with less organic matter and
2. To test how the presence of sulfate-depleted subsurface brine affects microbial communities, microbial activities, and microbial influence on environmental properties in organic-rich, sulfate-depleted sediments.

Site 1227 (427 m water depth) is in the immediate vicinity of Leg 112 Site 684, in a small fault-bounded sediment pond in the Trujillo Basin on the Peru continental shelf. The Trujillo Basin lies within the Peru upwelling zone, and its sediments are correspondingly rich in organic carbon. The total organic carbon (TOC) content of Site 684 sediment samples ranges between 1.2% and 10.6% (Shipboard Scientific Party, 1988). The average TOC concentration of these samples is approximately an order of magnitude higher than the average concentration at open-ocean Site 846 (Leg 201 Site 1226) (Shipboard Scientific Party, 1988, 1992a) and is about two orders of magnitude higher than the TOC content of open-ocean Site 851 (Leg 201 Site 1225) (Shipboard Scientific Party, 1988, 1992b).

¹Examples of how to reference the whole or part of this volume.

²Shipboard Scientific Party addresses.

Geochemical studies of Leg 112 sites show that brine is present below the seafloor in the Trujillo and Salaverry Basins (Suess, von Huene, et al., 1988). The composition of the brine differs from site to site, perhaps because of differences in its degree of dilution and the nature of its interaction with the surrounding sediments (Suess, von Huene, et al., 1988). Detailed chemical analyses indicate that this brine is of marine origin and is early Miocene in age (Kastner et al., 1990). The Leg 112 *Initial Reports* volume suggested that it enters the younger sediment column by diffusion from interstitial brine in underlying Miocene sediments (Suess, von Huene et al., 1988). Kastner and colleagues (1990) inferred that it is emplaced by stratigraphically bounded advection from north to south. The sulfate depletion of the brine at Site 1227 presumably results from bacterial sulfate reduction closer to the brine's source (e.g., deeper in the sediment column). Whatever the brine's mode of emplacement, Site 1227 provides an opportunity to study how the presence of sulfate-depleted brine affects subseafloor life in organic-rich sediments. Consequently, it provides an excellent standard of comparison for Sites 1228 and 1229, which are affected by the intrusion of sulfate-rich brine into, respectively, sulfate-bearing and sulfate-depleted sediments.

Leg 112 shipboard chemistry suggests that concentrations of methane at Site 684 increase by at least three orders of magnitude (from 10^2 to 10^5 $\mu\text{L/L}$) over the first 50 to 60 meters below seafloor (mbsf) and remain between 10^4 and 10^5 $\mu\text{L/L}$ to at least 100 mbsf. Ethane and butane concentrations also increase downhole to maximum concentrations at ~60 mbsf (Shipboard Scientific Party, 1988). In contrast, concentrations of dissolved sulfate decline from a near-seawater value to zero over the uppermost 30 or 40 mbsf (Shipboard Scientific Party, 1988). These profiles of dissolved hydrocarbons and sulfate indicate that the hydrocarbons and the sulfate are simultaneously destroyed by sulfate-reducing prokaryotic communities at ~40 mbsf.

Concentrations of several dissolved chemical species increase steadily to the base of the hole (ammonium, chloride, calcium, and magnesium). The increases in dissolved chloride, calcium, and magnesium provide evidence of the brine diffusing upward into the sediment column. Alkalinity exhibits a maximum value at ~40 mbsf, where the rate of anaerobic oxidation of methane appears to be greatest. The magnesium/calcium ratio peaks at 12 mbsf and steadily declines to the base of the hole, presumably as a result of dolomitization throughout the methane-rich sedimentary interval (Shipboard Scientific Party, 1988).

All of these patterns of sedimentary interstitial water concentration are inferred to result from relatively high levels of biological activity throughout the sediment column, coupled with diffusive exchange with the overlying ocean and with the brine introduced at depth. The subsurface extent of key electron donors (hydrogen, acetate, and formate) and electron acceptors with standard free-energy yields greater than that of sulfate (oxygen, nitrate, manganese oxide, and iron oxides) was not determined for Site 684.

PRINCIPAL RESULTS

Interstitial water studies at Site 1227 define one of the most highly resolved chemical records in Ocean Drilling Program (ODP) history. An important objective with these profiles is to identify and quantify zones of prokaryotic activity based on reactive interstitial water species. A

deep brine dominates the profiles of conservative seawater ions at this site, including chloride, which increases (with a linear gradient of 5 mM/m down to 70 mbsf and of 3 mM/m below that) to reach twice seawater chlorinity at 120 mbsf. Downhole depletion of sulfate at a relatively shallow depth, dissolved inorganic carbon (DIC) concentrations as high as 25 mM, ammonium rising to 23,000 μM at 150 mbsf, and very high concentrations of methane all indicate that prokaryotic activity is much higher at this ocean-margin site than at open-ocean Sites 1225 and 1226. Dissolved sulfate concentrations rapidly decline in the upper 15 mbsf from a seawater value of 29 mM to 5 mM. Concentrations then decline more slowly to 0 mM at ~40 mbsf. Concentrations of dissolved hydrogen sulfide ($\Sigma\text{H}_2\text{S} = \text{H}_2\text{S} + \text{HS}^-$) rise rapidly over the same 0- to 40-mbsf interval, from 0.04 mM at 0.24 mbsf to 9 mM at 39–40 mbsf. The convex-upward shape of both the sulfate and sulfide profiles from the sediment/water interface to ~40 mbsf indicates that bacterial sulfate reduction occurs throughout the interval. Sulfide concentrations steadily decline over the sulfate-poor remainder of the drilled section to <0.3 mM at 150 mbsf.

From 1 to 31 mbsf, dissolved barium concentrations rise slightly, from 0 to 1.9 μM . Over the next several meters, barium concentrations rise at an increasingly steep rate, climbing from 9 μM at 38 mbsf to 170 μM at 43 mbsf. Concentrations then rise steadily to 350 μM at ~150 mbsf. Dissolved sulfate and barium are both present throughout the entire interval of nonzero sulfate. Throughout this interval, the concentrations of dissolved barium and dissolved sulfate appear to be related by the solubility product of BaSO_4 (barite). Upward diffusion of barium from 43 to 38 mbsf appears to sustain modern barite formation in this Peruvian shelf sediment. The barite is visible as lighter bands in the sediment column and was confirmed by X-ray diffraction (XRD). At slightly greater depth (~42 mbsf), dissolved sulfate concentrations decline toward 0 mM, barite begins to dissolve, and dissolved barium concentrations rise. The narrow barium peak centered at 43 mbsf is inferred to mark the principal depth of current barite dissolution.

A similarly well-defined sulfate/methane interface coincides with the dissolved sulfide peak at ~40 mbsf. Dissolved methane concentrations slowly rise from 7 μM at 1 mbsf to 55 μM at 35 mbsf. From 40 to 56 mbsf, methane concentrations then rapidly rise to 2×10^3 μM at 56 mbsf and hover in the range of 10^3 μM for the remainder of the drilled sediment column. The disappearance of almost all methane at the depth of sulfate depletion indicates that most of the methane diffusing upward through this sediment column is ultimately destroyed by anaerobic methanotrophy. The presence of methane at a low concentrations throughout the overlying sediment column indicates, as at open-ocean Sites 1225 and 1226, that methane can be maintained at a background level of several micromolar in subseafloor sediments, despite the potential for methane oxidation by sulfate reduction.

Like methane, ethane and propane are detected throughout most of the sediment column. Ethane is present throughout the sediment column below ~1 mbsf, and propane is present throughout the column below ~11 mbsf. Concentrations of ethane decline sharply at the 40-mbsf top of the anaerobic methanotrophy zone (from 2 to 0.7 μM). Concentrations of propane decline more gradually (from 3 to 0 μM) in parallel with methane across the same interval. These distributions demonstrate that ethane and propane are biologically consumed in the anaerobic methanotrophy zone at this site. Concentrations of all three hydrocar-

bon species exhibit small distinct peaks in the upper part of the sulfate-rich zone. The presence of these small peaks demonstrates that methane, ethane, and propane are all biologically produced in sulfate-rich sediments at this site. Methanogenesis occurs at 1 mbsf, whereas ethanogenesis and propanogenesis occur at ~10 mbsf. Most of the methane, ethane, and propane produced in these sulfate-rich sediments are consumed within a few meters (~5 mbsf for methane and 15–25 mbsf for ethane and propane). Trace concentrations of the ethane (10^{-1} μM) persist throughout the sulfate-rich sediments at this site. This persistence indicates that ethane can be maintained at a very low background level in sulfate-rich sediments, despite its potential for oxidation by sulfate reduction.

In most incubation samples from Site 1227, hydrogen concentrations are between 0.2 and 0.5 nM. These concentrations closely resemble those observed at open-ocean Site 1226. Samples from the first few meters of the sediment column exhibit significantly higher hydrogen concentrations (0.9–2.4 nM). These concentrations are consistent with observation in shallower nearshore sediments (Hoehler et al., 1998). However, similar concentrations in samples from 93 and 113 mbsf are a factor of five to ten lower than those observed in nearshore methanogenic sediments. As for Site 1226, further investigation will be needed to determine whether or not these results indicate that the Site 1227 methanogenic and sulfate-reducing communities utilize hydrogen at free-energy yields lower than the generally accepted theoretical limit for actively growing cells.

The volatile fatty acids (VFAs) formate and acetate are important intermediates in the anaerobic pathways of organic matter degradation and were analyzed throughout the sediment column. Acetate concentrations range between 0 and ~10 μM and generally increase from the surface sediment down to the base of the drilled sediment column (~150 mbsf). Formate concentrations vary considerably throughout the sediment column (between 0 and ~5 μM) but exhibit no mean trend over the sampled sediment column. The average VFA concentrations of this site are an order of magnitude higher than concentrations in sediments of the equatorial Pacific sites and are similar to concentrations found in very active coastal marine sediments. These results suggest that relative substrate concentrations of different sites may be related to the activity levels of the principal prokaryotic processes, although the absolute process rates are orders of magnitude lower in the open-ocean sediments than in the coastal sediments.

Concentrations of dissolved manganese and iron are, respectively, 0–6 and 0–30 μM at Site 1227. The peak manganese concentration from Site 1227 (6 μM) is a factor of 27 lower than that of equatorial Pacific Site 1225 and a factor of 7 lower than that of equatorial Pacific Site 1226. The peak iron concentration from Site 1227 (30 μM) is a factor of 1.3 greater than that at Site 1225 and a factor of 1.5 lower than that at Site 1226. There are at least two possible explanations why the dissolved iron and manganese concentrations are low at Site 1227 relative to the open-ocean sites. Either the ferrimagnetic material at this ocean-margin site is not an effective source of bioavailable manganese and iron oxides, or dissolved manganese and iron are scavenged and precipitated much more quickly at this site. Stratigraphic relationships between magnetic susceptibility and dissolved sulfide concentrations suggest that these dissolved metals are scavenged by sulfide precipitation at Site 1227. A relatively steep decline in sulfide concentrations from 40 to 75 mbsf is associated with the prominent magnetic susceptibility peak

from 40 to 50 mbsf. The ultimate sink for sulfide diffusing deeper into the column is associated with the other most prominent magnetic susceptibility peak at this site (which begins at ~140 mbsf).

A pronounced peak in the value of almost every physical property measured at this site spans the interval from 40 to 50 mbsf. These physical properties include magnetic susceptibility, gamma ray attenuation (GRA) bulk density, grain density, *P*-wave velocity, natural gamma radiation (NGR), thermal conductivity, and axial formation factor. Smaller peaks in the values of most of these properties are present in the uppermost 20 m of the sediment column. The bulk porosity profile mirrors the variability in other physical properties at this site; its downhole record is nearly the exact inverse of the bulk density and grain density records. These variations in physical properties result from variations in the bulk lithology of the sediment column. The porosity lows and high values in other physical properties are present in sandier intervals of the sediment column.

The 40- to 50-mbsf interval is composed of sandy silt, rich in glauconite, dolomite, quartz, feldspar, pyrite, and shell fragments. It grades upward into dolomite-bearing clayey silt, rich in diatoms and nanofossils. It directly overlies clay- and nanofossil-bearing diatom ooze. Traces of bioturbation are much more abundant in the 40- to 50-mbsf interval than in the overlying and underlying sediments. The primary front of active anaerobic methanotrophy occurs at the top of this 40- to 50-mbsf sandy interval. The successive fronts of barite precipitation and barite dissolution are present in the same interval. Peak concentrations of dissolved iron, manganese, silica, and phosphate are also present in this interval. Secondary peaks in the dissolved concentrations of iron, manganese, silica, and phosphate are present between 0 and 20 mbsf and are similarly associated with relatively coarse-grained sediments. These relationships suggest that several principal activities of the subsurface biosphere (including anaerobic methanotrophy, iron and manganese reduction, ethanotrophy, and propanotrophy) are pinned in a narrow stratigraphic interval by physical properties and sediment composition at this site. The mineral composition and traces of relatively intensive bioturbation indicate that the physical and compositional properties of this interval are primarily determined by the nature of the sediment when it was first deposited on the seafloor. However, to some extent, these properties may have been modified by the postdepositional microbial activities that still occur in them today. Density and porosity can be affected by biologically mediated precipitation and dissolution of authigenic minerals, such as barite, dolomite, and apatite. Magnetic susceptibility may be diminished by biologically mediated dissolution of solid-phase iron oxides and subsequent iron reduction. To a much lesser extent, magnetic susceptibility may also be enhanced by biologically induced precipitation of reduced iron and manganese. More detailed determination of the extent to which physical and compositional properties control the microbial activities at this site and the extent to which those activities control the physical and compositional properties will require further investigation.

Preliminary cell counts of eight samples from Site 1227 suggest that sedimentary cell concentrations at most sediment depths are slightly higher at this ocean-margin site than at equatorial Pacific Site 1225. Based on the same few data, at most sediment depths, cell concentrations from Site 1227 may be roughly equivalent to those of open-ocean Site 1226. This data set will be expanded by postcruise analyses.

Experiments on major microbial processes and on enumeration of viable prokaryotes were initiated at selected depths ranging from near the mudline to the bottom of the drilled sediment column. The studied processes include methane and acetate formation and consumption, sulfate reduction, hydrogen oxidation, and rates of cell growth. The cultivation experiments include selective growth conditions for a wide range of autotrophic and heterotrophic prokaryotes ranging from psychrophilic to thermophilic. Specific sampling was targeted to the sulfate/barium interface to study the possible attack of sulfate-reducing bacteria and methane-oxidizing archaea on sulfate bound in barite.

One Adara and two Davis-Villinger Temperature Probe (DVTP) deployments combined with the Leg 112 data define a linear gradient of 49°C/km, with a sediment/water interface temperature of 8.6°C and an estimated temperature at 160 mbsf of 16.4°C. Throughout the sediment column, temperatures are in the low mesophilic range.

Trials were undertaken of three experimental tools at this hole: the pressure coring sampler (PCS), the DVTP with pressure (DVTP-P), the Fugro Percussion Corer (FPC), and the APC-Methane (APC-M) tool.

OPERATIONS

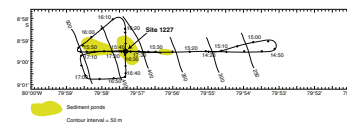
Transit to Site 1227

We made the 745-nmi transit between Sites 1226 and 1227 in 63.7 hr at an average speed of 11.7 kt, arriving on location at ~0800 hr on 28 February. Because our drilling target was a small sediment pond, we decided to conduct a brief 3.5-kHz survey in a west-east then north-south cross pattern centered on our projected site coordinates to confirm our position (Fig. F1). On the first west-east limb of our survey (based on coordinates reported on the first page of the Leg 112 *Initial Reports* volume Site 684 report [Shipboard Scientific Party, 1988]), we were concerned that the seafloor depth indicated by the survey was significantly shallower than the reported depths at Site 684 (~250 m as opposed to 426 m). In addition, the survey showed no evidence of sediment cover. At this point, we noticed a 3-nmi discrepancy between the coordinates reported in the Leg 112 *Initial Reports* volume and the site survey navigation track for Site 684 presented later in the chapter. The ODP Drilling Services Department operations report for Leg 112 records coordinates that agree with the Site 684 site survey data, so we moved our survey location center to these coordinates. The water depth at our new survey location agreed with the water depth reported in the Leg 112 *Initial Reports* volume, and our survey indicated the presence of a sediment pond, although the limited penetration of the 3.5-kHz signal below the seafloor did not allow us to estimate the sediment thickness. Based on our survey data, we selected a position 50 m north of the Site 684 survey coordinates to begin coring operations at Site 1227. Prior to initiating coring, we affected a personnel and equipment transfer via a Peruvian Navy helicopter. Coring operations at Site 1227 are summarized in Table T1.

Hole 1227A

Operations in this hole began with deployment of the Water Sampling Temperature Probe (WSTP) to collect a bottom-water sample and a near-mudline water temperature. Upon recovery of the WSTP, we no-

F1. Site 1227 survey, p. 29.



T1. Coring summary, p. 57.

ticed the probe tip had mud impacted in the water sample ports, suggesting that either the tool had embedded below the mudline or the interface between the seafloor and sediment column was turbid. Core 1H established the mudline at 438.9 mbrf. While planning for shallow-water drilling at all of the Peru margin sites, we recognized that the drill crew could deliver cores to the core laboratory at a much faster rate than the cores could be processed, owing to the high-resolution geochemistry we required and the core handling requirements for microbiological sampling. To account for protracted laboratory handling times, we initiated a protocol of slowing core recovery, which required continual communication between the various processing laboratories and the rig floor. In short, coring operations were held in stasis by the drilling crew until word was received from both the chemistry and microbiology processing groups that they were approaching the end of a sample handling program. The rig floor crew would then respond with immediate deployment of the next core barrel. This routine prevented cores from piling up in the laboratories, enhancing our chances of meeting our science objectives.

The first five advanced hydraulic piston coring (APC) cores (Cores 1H through 5H) (0.0–43.6 mbsf) returned 105% recovery. Hydrogen sulfide monitoring registered measurable quantities of hydrogen sulfide on core surfaces beginning with Core 2H, and levels rose to as high as 25 ppm in the first few cores. Hydrogen sulfide core handling protocols were initiated after Core 2H. It is important to note that the core handling procedures dictated by safety have a potential impact on science objectives because they may slow delivery of samples to the microbiology and geochemistry laboratories. Consequently, biogeochemical and microbiological samples were processed as rapidly as possible while adhering to hydrogen sulfide safety protocols. In addition, hydrogen sulfide was continuously monitored in all laboratories. Core flow through the physical property and description laboratories was radically slowed because even after perforating the cores, residue of as much as several parts per million of hydrogen sulfide was detectable in core sections several hours after recovery.

Recovery began to deteriorate after Core 5H, as the next several APC barrels (Cores 6H through 8H; 43.6–72.1 mbsf) returned an average of 40%. Through this interval, recovery ranged from as little as 4% to as much as ~70%. In addition, starting with Core 8H we were required to drill over the APC shoe when we encountered elevated tension when trying to extract core barrels via wireline (overpull). However, we chose to continue to attempt APC coring to as deep as possible, since the extended core barrel (XCB) cores we had recovered from previous sites were so disturbed and XCB coring during Leg 112 had experienced such poor recovery (average = <15% at this location). After Core 8H and continuing through the bottom of the hole (Cores 9H through 18H; 72.1–151.1 mbsf) recovery improved to average of 60%, which allowed us much improved core recovery and quality as compared to operations during Leg 112. Hole 1227A was terminated after impacting a hard layer at 151 mbsf in Core 18H.

Several downhole tool measurements were accommodated by our slowed recovery pace in Hole 1227A. The Adara temperature shoe was deployed on Core 4H. Because the core liner from Core 4H shattered, possibly as a result of the measurement protocol, we abandoned Adara tool measurements in lieu of DVTP runs for the remainder of the hole. The DVTP was deployed at 81.6 and 110.1 mbsf, and the DVTP-P was deployed at 132.1 mbsf. Both the PCS and the FPC were deployed be-

tween 128 and 132 mbsf, but neither run was particularly successful, as the only material recovered was a handful of pebbles and shell hash. The APC-M tool was deployed on Cores 4H and 5H. The WSTP was deployed once each above Holes 1227A and 1227D with failure on the first run and success on the second run.

Holes 1227B, 1227C, 1227D, and 1227E

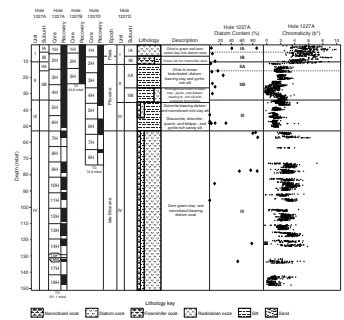
Holes 1227B, 1227C, and 1227E were all three-core holes (mudline plus two subsequent penetrations) dedicated to shipboard and shore-based high-resolution sampling. Hole 1227D was drilled to provide high-resolution microbiological and geochemistry sampling and to attempt to improve recovery rates in certain intervals cored in Hole 1227A. Our target depth for this hole was to reach the interval at ~70 mbsf, where recovery improved while APC coring in Hole 1227A. Cores 201-1227D-1H through 5H (0.0–45.5 mbsf) returned 96% recovery. Core 201-1227D-6H (45.5–55.0 mbsf) was nearly full (recovery = 96%), but a shattered core liner resulted in severe core disturbance in the lower two-thirds of the core. Core 201-1227D-7H also returned with a shattered core liner and only a handful of pebbles and shell hash. In addition, the end of the APC cutting shoe showed evidence of impact with a hard ground. Coring operations were terminated in Hole 1227D when Core 201-1227D-8H (64.5–74 mbsf) delivered an incomplete stroke and returned only 1.7 m of core. The APC-M tool was deployed on Cores 201-1227D-1H through 7H.

After recovering three cores from Hole 1227E (Cores 201-1227E-1H through 3H) (0.0–25.9 mbsf; recovery = 101%) that were not split and that were end-capped without acetone but with tape, we deployed the FPC. This strategy allowed a test of the FPC in an interval where we were confident that the lithology contained more abundant clay and less abundant sand and pebbles. Operations at Site 1227 concluded when the bit passed through the rig floor at 0245 hr on 3 March, and we began a short transit to Site 1228.

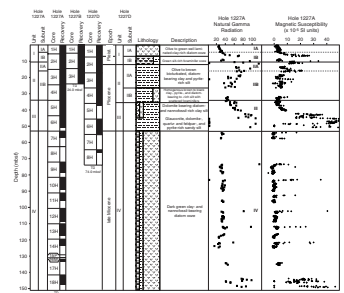
LITHOSTRATIGRAPHY

At Site 1227, we recovered a 151-m-thick sequence of alternating diatomaceous and siliciclastic sedimentary packets. Lithologic, textural, and compositional variations observed in these sediments justify subdivision into four lithostratigraphic units (Fig. F2). The proposed lithostratigraphy framework is mostly based on Hole 1227A, as it was the only hole at Site 1227 that was continuously cored from the sediment surface to a depth of 151.1 mbsf. The lithostratigraphic description of the sedimentary sequence is based on visual observation of sediment color and sedimentary structures (visual core description), smear slide analysis, and color reflectance. XRD and laboratory measurements of magnetic susceptibility, density, and natural gamma ray (see “Physical Properties,” p. 21) were also used to detect lithologic changes (Fig. F3). As Site 1227 is located in close proximity (within 100 m) of Site 684, which had previously been drilled during Leg 112, the age framework presented in this chapter was obtained by applying the timescale of Berggren et al. (1995a, 1995b) to the magnetostratigraphic and biostratigraphic observations of the Leg 112 Shipboard Scientific Party (1988).

F2. Lithostratigraphic summary, p. 30.



F3. Lithostratigraphy with magnetic susceptibility and NGR, p. 31.



Description of Lithostratigraphic Units

Unit I

Interval: 201-1227A-1H-1 through 2H-4 and 201-1227D-1H-1 through 2H-6

Depth: 0–11.1 mbsf (Hole 1227A) and 0–14.6 mbsf (Hole 1227D)

Age: Pleistocene

The main lithology of Unit I consists of well-laminated olive silt- and clay-rich diatom ooze. In the lower part of the unit, two coarse-grained green to dark olive diatom-bearing, silt-rich foraminifer ooze layers alternate with laminated clay-bearing diatom ooze. The laminated interval between the two foraminifer ooze layers ranges between 2.0 and 2.6 m thick. These differences in lithology and texture between the upper and the lower part of Unit I account for its subdivision into Subunits, IA and IB (Fig. F2).

Subunit IA

Interval: 201-1227A-1H-1 through 2H-1 and 201-1227D-1H-1 through 1H-5

Depth: 0–6.2 mbsf (Hole 1227A) and 0–6 mbsf (Hole 1227D)

Subunit IA consists of mostly olive to green clay-rich diatom ooze characterized by very fine scale lamination (laminae range from <1 mm to a few millimeters in thickness). Most of the laminae show parallel bedding; however, the presence of low-angle laminations and pinch-out terminations of sedimentary layers seems to indicate some reworking by bottom currents (Fig. F4A). Coarser and lighter-colored laminae are usually richer in opal-A diatom frustules, whereas darker foraminifer-bearing laminae are composed of calcite, quartz, and feldspars. Fish scales and vertebra as well as crab debris are locally present in these sediments. Subunit IA corresponds to a low magnetic susceptibility zone (Fig. F3).

Subunit IB

Interval: 201-1227A-2H-2 through 2H-4 and 201-1227D-1H-5 through 2H-2

Depth: 6.2–11.1 mbsf (Hole 1227A) and 6–10.5 mbsf (Hole 1227D)

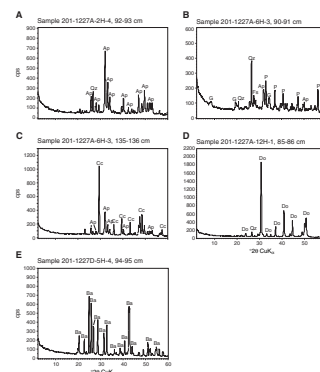
The diatom ooze of the overlying Subunit IA grades into a dark olive to green silt-rich foraminifer ooze containing scattered shell debris as well as small thick-walled taxodont bivalves (Fig. F4B). The foraminifers are mostly benthic. A bone fragment was found in Section 201-1227A-2H-1 at 39 cm (Fig. F4C). Sediments of Subunit IB are characterized by a pronounced excursion in magnetic susceptibility, natural gamma radiation, and density (Fig. F3).

Near the base of Section 201-1227D-2H-2, a ~15-cm-thick phosphatic hardground defines the base of Subunit IB (see “Mineralogy,” p. 12; XRD results for Sample 201-1227D-2H-2, 139–140 cm). The phosphate is black and hard (D-phosphate, according to the Leg 112 classification; Shipboard Scientific Party, 1988) and replaces a burrowed interval. Phosphate nodules composed of carbonate fluorapatite are also present in Section 201-1227A-2H-4 (Fig. F5A). The transition to Unit II is marked by a pronounced shift in the chromaticity (b^*) data toward lower values (Fig. F2).

F4. Site 1227 features, p. 32.



F5. X-ray diffractograms, p. 34.



Unit II

Interval: 201-1227A-2H-4 through 4H-CC and 201-1227D-2H-6 through 4H-CC

Depth: 11.1–34.1 mbsf (Hole 1227A) and 14.6–36 mbsf (Hole 1227D)

Age: Pliocene

Unit II at Site 1227 consists of dark olive-brown to black bioturbated silty sediments. Glauconite and phosphate grains are common. Based on variations in diatom content, two subunits were established within Unit II. Subunit IIA is characterized by low diatom concentrations (<5%), whereas the sediments of Subunit IIB show diatom contents of up to 25% as well as small amounts of biogenic carbonate (mostly foraminifers) (Fig. F2). The boundary between the two subunits is not sharp but rather is a gradual transition from an almost pure siliciclastic interval to sediments containing greater amounts of biogenic silica.

Subunit IIA

Interval: 201-1227A-2H-4 through 2H-CC and 201-1227D-2H-6 through 3H-CC

Depth: 11.1–15.4 mbsf (Hole 1227A) and 14.6–26.5 mbsf (Hole 1227D)

The dominant lithology of Subunit IIA is a dark olive-brown bioturbated diatom-bearing clay- and pyrite-rich silt. In Section 201-1227A-2H-4, the contact between the overlying coarser-grained foraminifer ooze of Subunit IA and the dark brown diatom-bearing silt of Subunit IIA is sharp, and two black phosphate nodules (Figs. F3, F4D; XRD results for Sample 201-1227-2H-4, 92–93 cm) were observed. Variable amounts of quartz and glauconitic components were detected in sediment-filled burrows.

Natural gamma radiation and magnetic susceptibility data for this subunit (Fig. F3; see also “Physical Properties,” p. 21) show a prominent peak. These high values probably reflect a relatively high content of terrigenous components as well as a concentration of an unknown magnetic mineral in Subunit IIA.

Subunit IIB

Interval: 201-1227A-3H-1 through 4H-CC and 201-1227D-4H-1 through 4H-CC

Depth: 15.4–34.1 mbsf (Hole 1227A) and 26.5–36.0 mbsf (Hole 1227D)

Age: Pliocene

Subunit IIB was distinguished from overlying Subunit IIA based on higher amounts of diatom frustules, fewer clastic components, and darker color. The main lithology consists of homogeneous to slightly bioturbated dark brown to black clay-, pyrite-, and diatom-bearing to diatom-rich silt with scattered sand-sized benthic foraminifers. At Section 201-1227A-4H-5, 62 cm, a lighter-colored calcite-cemented layer is present (XRD Sample 201-1227A-2H-4, 92–93 cm). Pyritized radiolarian and foraminiferal tests are common. In interval 201-1227D-4H-5, 90–110 cm, two vertical veinlets of a very fine grained barite are present (Fig. F4E) (see also “Mineralogy,” p. 12, and XRD results for Samples 201-1227D-4H-5, 100–101 cm, and 5H-4, 94–95 cm). The uppermost bound-

ary of Subunit IIB is marked by a sudden decrease in both natural gamma radiation and magnetic susceptibility (Fig. F3) (see also “**Physical Properties**,” p. 21), which probably reflects a decrease of terrigenous input and lower concentrations of magnetic minerals.

Unit III

Interval: 201-1227A-5H-1 through 6H-5 and 201-1227D-5H-1 through 6H-CC
Depth: 34.1–53.1 mbsf (Hole 1227A) and 36.0–55.0 mbsf (Hole 1227D)
Age: Pliocene

A reduction of the diatom component (Fig. F2) and a parallel increase of clay, quartz, feldspar, silt-sized pyrite, and glauconite characterize this unit. Two main lithologies, dolomite-bearing diatom- and nannofossil-rich clayey silt and dark brown dolomite-, quartz-, feldspar-, and pyrite-rich sandy silt with scattered foraminifers and variable amounts of glauconite, characterize the uppermost and the lowermost part of this subunit, respectively. The concentration of glauconitic clasts as well as the grain size of the sediment varies throughout the unit. Both fining- and coarsening-upward sequences are common (e.g., the top of Section 201-1127A-6H-2 consists of silt-sized pyrite and glauconitic grains, whereas the bottom is a diatom-rich clay). However, diatom-rich clay is mostly present in the upper part of the unit, and clasts tend to be coarser toward the bottom of the unit, where both sand grains and millimeter- to centimeter-sized shell fragments are common. Evidence of bioturbation also appears to be more intensive in the lower part of the unit (i.e., below 45 mbsf in Hole 1227A). Usually, bioturbated intervals were found near the boundaries between layers of different grain size, where they are manifested by mottles and burrows of silty/sandy sediment in clayey/silty layers and vice versa. Section 201-1227A-6H-3 contains a reddish brown diatom-rich layer that includes a pale pink lens composed of calcite and apatite (Fig. F5C) (see also “**Mineralogy**,” p. 12).

The fining-upward trend observed in Unit III is also reflected by a significant decrease in both magnetic susceptibility and natural gamma radiation (Fig. F3) (see also “**Physical Properties**,” p. 21). In particular, both parameters show a peak between 40 and 51 mbsf, where most of the silt and sand layers are also concentrated. A similar parallelism between positive excursions in grain size, magnetic susceptibility, and natural gamma radiation was already observed in Subunit IB.

Unit IV

Interval: 201-1227A-7H-1 through 18H-CC and 201-1227D-7H-1 through 8H-CC
Depth: 53.1–151.1 mbsf (Hole 1227A) and 55.0–74.0 mbsf (Hole 1227D)
Age: late Miocene

The main lithology of Unit IV is a dark green clay- and nannofossil-bearing diatom ooze (Fig. F2). According to the biostratigraphic determinations from Site 684, the boundary between Units III and IV corresponds to a major stratigraphic hiatus (Shipboard Scientific Party, 1988). In particular, nannoplankton data indicate that this stratigraphic gap

ranges between 5.7 and 8.7 Ma (Shipboard Scientific Party, 1988, modified after Berggren et al., 1995b). The sediment is generally homogenous and contains only a few scattered laminated or bioturbated layers. Volcanic ash layers and dark volcanic glass shards are present throughout the unit. Section 201-1227A-12H-1 contains a laminated dolomite nodule at a depth of 85 cm in the section (Fig. F5D). The core catcher of Core 201-1227A-8H contained gravel-sized dark green, olive (probably phosphate), and white (probably dolomite) clasts, mixed with shell hash and olive-green nannofossil- and clay-bearing diatom ooze. Gravel of the same composition as the gravel recovered in Core 201-2117A-8H was found in the first 30–40 cm of every subsequent core, which strongly indicates that the presence of gravel at the tops of Cores 201-1227A-9H through 18H is, in fact, a drilling artifact. The sediments in Cores 201-1227A-12H and 13H are diatom poor and consist mostly of dark olive-green to brown clay and silt (Fig. F2). Below Core 201-1227A-14H, both recovery and preservation of the cores were very poor (Fig. F2).

Mineralogy

X-ray diffraction analyses were performed on 19 samples from Site 1227. XRD spectra of the main sedimentary components confirm the results of visual core descriptions and smear slide analyses. Biogenic opal-A and calcite dominate the composition of the foraminifer-bearing diatom-rich sediments of Subunits IB and IIA and Unit III. Pyrite is common throughout the sedimentary section (e.g., XRD results for Sample 201-1227A-6H-3, 90–91 cm) (Fig. F5B).

XRD analyses confirmed the presence of various diagenetic minerals in Site 1227 sediments. As already noted by the Leg 112 Shipboard Scientific Party (1988), there appears to be a close association between depositional environment and the formation of certain diagenetic mineral assemblages at Site 1227. Authigenic carbonate nodules are closely associated with diatom-rich upwelling-derived sediments, whereas massive phosphates and glauconite appear to be associated with sediments that were deposited in a shallower, current-dominated environment.

Black, hard nodules of apatite and carbonate fluorapatite (D-phosphate, according to Leg 112 classification; Shipboard Scientific Party, 1988) define the base of Subunit IB at Site 1227 (Fig. F5A; XRD results for Samples 201-1227A-2H-4, 92–93 cm, and 201-1227D-2H-2, 139–140 cm).

Phosphate nodules composed of apatite and carbonate fluorapatite are also present in Unit III (XRD results for Sample 201-1227A-6H-3, 92–93 cm). The formation of these D-phosphate nodules has been attributed to variable and high-energy conditions during past sea level lowstands (Garrison and Kastner, 1990).

Carbonate nodules are more common in sediments dominated by biogenic components. XRD analysis of a laminated carbonate nodule from Unit IV (XRD results for Sample 201-1227A-12H-1, 85–86 cm) revealed the presence of dolomite (Fig. F5D). Authigenic calcite was also observed (e.g., XRD results for Sample 201-1227A-6H-3, 135–136 cm) (Fig. F5C). For a detailed discussion of the diagenetic environment at Site 1227, see Shipboard Scientific Party (1988) and Garrison and Kastner (1990).

Thin white veinlets and nodules of authigenic barite were observed in Hole 1227D at depths between 33.5 and 45.6 mbsf (XRD results for Samples 201-1227D-4H-5, 100–101 cm; 5H-4, 94–95 cm; and 6H-1, 15–16 cm) (Fig. F5E). XRD spectra point to strontian barite as the main bar-

ite mineral. The presence of barite is closely tied to the interstitial water sulfate, barium, and methane cycle at Site 1227. Barite is inferred to form in Site 1227 sediments when interstitial water sulfate levels approach concentrations around ~2 mM, due to anaerobic oxidation of methane (see “**Biogeochemistry**,” p. 13). This in turn triggers barite precipitation and the formation of a “barite front” near the base of the sulfate reduction zone.

Summary

The sedimentary sequence at Site 1227 consists of large-scale alternations of predominantly biogenic sediments, formed in an upwelling environment analogous to today’s conditions along the Peruvian continental margin (Unit I, lower part of Unit II [Subunit IIB], and Unit IV), and sediments that are dominated by siliciclastic components, indicating deposition in sedimentary environments different from modern conditions (Unit II [Subunit IIA] and Unit III). Lithostratigraphic Unit I consists of laminated olive silt- and clay-rich sediments dominated by diatoms. In the lower part of the unit, two coarse-grained green to dark olive diatom-bearing silt-rich foraminifer ooze layers alternate with laminated clay-bearing diatom ooze. Unit II is dominated by dark olive-brown to black bioturbated silty sediments. Based on variations in diatom content, two subunits were established. Subunit IIA is characterized by low diatom concentrations, whereas the sediments of Subunit IIB show, on average, higher diatom content as well as small amounts of biogenic carbonate. The boundary between the two subunits is not sharp but rather is a gradual transition from an almost pure siliciclastic interval to sediments containing greater amounts of biogenic silica. The upper part of Unit III is characterized by dolomite-bearing diatom- and nannofossil-rich clayey silt, whereas the lower part is mostly a dark brown dolomite-, quartz-, feldspar-, and pyrite-rich sandy silt with scattered foraminifers and variable amounts of glauconite. Dark green clay- and nannofossil-bearing diatomaceous sediments characterize Unit IV. The sediment is generally homogeneous and contains only a few scattered laminated or bioturbated layers. Volcanic ash layers and dark volcanic glass shards are present throughout the unit. Material of the same composition as the gravel layer recovered in Section 201-2117A-8H-CC was found in the top of every subsequent core, which strongly indicates that the presence of gravel in core tops below ~65 mbsf is due to drilling artifacts. Below Core 201-1227A-14H, both recovery and preservation of the cores were very poor.

Diagenetic processes in Site 1227 sediments caused the formation of authigenic phosphates (apatite and carbonate fluorapatite), carbonates (calcite and dolomite), and barite. The formation of different diagenetic minerals can be correlated to distinct geochemical and/or sedimentary environments, such as ongoing anaerobic oxidation of methane or changes in oceanographic conditions (sea level fluctuations) during the last 11 m.y.

BIOGEOCHEMISTRY

The interstitial water (IW) sampling strategy for Site 1227 was designed to determine chemical profiles at high vertical resolution for comparison with Sites 1228 and 1229. The aim was to resolve the biogeochemical processes occurring in these deeply buried marine sedi-

ments where subsurface brines influence interstitial water chemistry. In Hole 1227A, IW samples were taken from each section of Cores 201-1227A-1H through 5H, with the exception of Core 4H (two samples), down to 42.95 mbsf. The sampling frequency was reduced to three IW samples in Core 201-1227A-6H and two IW samples per core below Core 6H down to the maximum penetration depth. Low recovery in Cores 201-1227A-14H and 16H allowed subsampling of only one IW sample from each. A total of 42 IW samples down to 144.45 mbsf were taken from Hole 1227A. An additional 18 IW samples collected from Hole 1227D targeted specific intervals of interest. One was the sediment/water interface, with five samples collected from 0.00 to 1.80 mbsf in Section 201-1227D-1H-1. Another was the sulfate–methane transition in Cores 201-1227D-4H and 5H from 27.85 to 42.91 mbsf (Table T2), with six samples collected from Core 4H and five from Core 5H. Analysis of this interval in Hole 1227A had shown the depletion of dissolved sulfate and the presence of elevated levels of dissolved methane and barium. In addition to routinely employed chemical analyses, we acquired IW concentration data for hydrogen, acetate, formate, total inorganic carbon, manganese, iron, and headspace methane.

Alkalinity and DIC have similar profiles downhole. Alkalinity increases steeply from 3.3 mM near the sediment/water interface to a maximum of ~24 mM at 41.5 mbsf, below which it decreases to ~22 mM at 49.45 mbsf (Fig. F6A). After an ~6 mM offset to lower concentrations between 49.45 and 54.45 mbsf, concentrations are between 14 and 19 mM to the bottom of Hole 1227A. The range in alkalinity at this site is ~21 mM. DIC exhibits a similar profile, with values increasing from 3.2 mM near the sediment/water interface to a maximum of 23 mM at 42 mbsf (Fig. F6B). The DIC concentration decreases to ~18 mM at the bottom of Hole 1227A with a similar offset between 49.45 and 54.45 mbsf. The range in DIC concentration is ~26 mM.

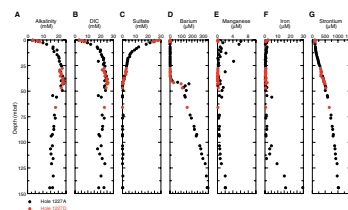
Maximum alkalinity and DIC concentrations at Site 1227 are considerably higher than those at open-ocean Sites 1225 and 1226. These higher values strongly suggest that rates of microbial activity are higher at Site 1227 than at the open-ocean sites. TOC content is generally high, with values ranging from 1% to >10% (Table T7, p. 97; Fig. F6A, p. 54, both in the “Site 1230” chapter). These high concentrations of organic carbon largely derived from algal debris (hydrogen index values of up to 500 mg HC/g TOC (Table T7, p. 97, in the “Site 1230” chapter) support the high microbial activity at Site 1227.

Sulfate penetrates to 42 mbsf, below which the concentrations remain at or near zero (Fig. F6C). Nonzero values at depths below 42 mbsf are assumed to be due to slight seawater contamination during drilling or sulfide oxidation during sampling. The sulfate profile over the uppermost 42 mbsf is complex. Sulfate concentrations drop steeply from the seawater value of 28.9 mM near the sediment/water interface to ~6 mM at 15 mbsf, probably indicating high rates of sulfate reduction in the upper sediment column. Between 15 and 42 mbsf, the gradient is less steep and includes an ~1-mM offset at ~35 mbsf. Sulfate overlaps with upward-migrating methane from 36 to 42 mbsf. Most anaerobic oxidation of methane takes place in this interval at this site. There is similar overlap between sulfate and upward-diffusing dissolved barium over the same depth interval.

Interstitial water barium concentrations (Fig. F6D) change in accordance with the sulfate distribution and may be controlled by barite solubility. Barium is close to the detection limit (~0.1 μM) near the sediment/water interface and slowly rises to 2 μM at 35 mbsf. Below this

T2. Dissolved species in interstitial waters, p. 59.

F6. Dissolved species in interstitial waters, p. 35.



depth, which coincides with a major increase in headspace methane, dissolved barium concentrations increase by over two orders of magnitude to nearly 346 μM at 145 mbsf. This rise is not steady but includes a prominent peak at 43 mbsf. The barium profile provides evidence for a zone of barite dissolution in the upper portion of the sulfate–methane transition and a zone of barite precipitation immediately below the sulfate/methane interface. White veinlets and layers, confirmed as barite by XRD, were found at 33.5 mbsf (see “**Mineralogy**,” p. 12, in “Lithostratigraphy”). The dissolved barium profile around the sulfate/methane interface may indicate that the upward migration methane has increased in the recent past (Dickens, 2001).

In contrast to the deep-sea Sites 1225 and 1226, the dissolved manganese profile at Site 1227 (Fig. F6E) shows considerable scatter and low concentrations (0–7 μM) over the upper 60 mbsf. Below 66 mbsf, dissolved manganese concentrations slowly rise to 2 μM at 145 mbsf. Site 1227 is located at the lower boundary of a strong oxygen minimum zone in the overlying water column. Solid manganese probably becomes reduced and dissolves in the upper few centimeters of the sediment column or water column, which minimizes burial of solid manganese in the sediment.

Dissolved iron concentrations (Fig. F6F) remain near the detection limit (~ 0.2 μM) down to ~ 100 mbsf with two exceptions. The upper 2 mbsf shows a 2- μM decrease, and a few samples between 45 and 65 mbsf have concentrations of 2–5 μM . Below 100 mbsf, dissolved iron concentrations rise to 30 μM . Dissolved iron concentrations are limited by sulfide solubility and the dissolved sulfide distribution. Most of the labile iron entering the sediment column probably precipitates as sulfides.

Dissolved strontium concentrations (Fig. F6G) rise from 90 μM at the seafloor to 1025 μM at 145 mbsf. Unlike chloride, however, the profile is not linear but has concave-upward curvature between the seafloor and ~ 50 mbsf and concave-downward curvature between 50 and 144 mbsf. A prominent 50- μM drop in strontium is also present at ~ 35 mbsf. The overall 6.45- $\mu\text{M}/\text{m}$ rise in strontium is one of the most extreme strontium gradients recorded in the marine realm and implies a substantial flux of strontium from deep brines along the Peru margin to shallow sediment and seawater. The curvature in the strontium profile from 0 to 25 mbsf and the marked deviation at ~ 35 mbsf probably reflect zones of local strontium removal to carbonate and barite, respectively.

Dissolved lithium concentrations (Fig. F6H) rise from 27 μM near the seafloor to 1435 μM near the bottom of the hole. At nearly 10 $\mu\text{M}/\text{m}$, the increase in lithium is even greater than that for strontium. Its profile is less curved than that of strontium. As with strontium, there is a substantial flux of lithium from deep brines along the Peru margin to shallow sediment and seawater.

Total dissolved sulfide ($\Sigma\text{H}_2\text{S} = \text{H}_2\text{S} + \text{HS}^-$) is present at a concentration >0.043 mM in the uppermost 0.24 mbsf and increases with increasing depth to a peak concentration of ~ 9 mM at 38.9 mbsf (Fig. F6I). The sulfide peak coincides with the depth of the sulfate/methane interface. The shape of the sulfide curve over the 0- to 38-mbsf interval is convex upward, which suggests sulfide production via bacterial sulfate reduction throughout this interval. Below 38.9 mbsf, dissolved sulfide concentrations abruptly decrease with increasing depth. The general concave-downward shape of the sulfide profile between 40 and 75 mbsf suggests removal of sulfide, perhaps due to reactions with iron

minerals (see “**Magnetic Susceptibility**,” p. 22, in “Physical Properties”). Below 75 mbsf, sulfide concentrations decrease steadily to 0 mM at 144 mbsf.

Acetate and formate were analyzed in 30 IW samples from Holes 1227A and 1227D and 12 samples from Hole 1227D to better define their concentrations in intervals where sulfate decreases (Table T2; Fig. F6J, F6K). Concentrations of both species are generally higher than those at Sites 1225 and 1226, with the exception of the lowermost 80 m of Site 1226 (see “**Biogeochemistry**,” p. 14, in the “Site 1225” chapter and “**Biogeochemistry**,” p. 13, in the “Site 1226” chapter). Minimum concentrations of acetate exist in two intervals. The first of these intervals is the upper 10 mbsf and the second is from 30 to 50 mbsf. These two intervals include the two depth zones where the sulfate profile suggests maximum rates of sulfate reduction. Apart from these two intervals, acetate concentrations rise with increasing burial depth—a general trend also noted at Site 1226. Acetate concentrations below 100 mbsf are 3.5–6 μM . With regard to minimum concentrations, the profile of formate resembles that of acetate except that the overall variability in formate is higher than that of acetate (Fig. F6K). In the majority of samples, formate concentrations are $<3 \mu\text{M}$. In contrast to acetate, no significant downhole increase in formate concentrations is evident.

Methane was detected in all samples at Site 1227 (Table T3; Fig. F6L). Methane concentrations increase steadily with depth and reach 55 μM in the sulfate–methane transition zone (~35–38 mbsf). In more deeply buried sediments, methane concentrations increase sharply and reach a plateau of maximum concentration below a depth of 47.9 mbsf. Below that depth, concentrations vary from ~0 to 3400 μM . We suggest that these changes reflect changes in lithology and corresponding effects on methane degassing upon core retrieval rather than “real” changes in interstitial water concentrations of methane (Paull, Matsumoto, Wallace, and Dillon, 2000).

Low concentrations of ethane and propane were detected in the majority of the samples, with ethane concentrations reaching a maximum of ~3 μM (Fig. F6M). The overall depth profile of ethane approximately tracks that of methane, although the methane/ethane ratio increases from ~50 between 10 and 30 mbsf to values $>10^3$ below 50 mbsf (Fig. F6N). Notably, there are lows in ethane concentrations and the methane/ethane ratio at ~35 mbsf. This suggests that some fraction of ethane is consumed in the sulfate–methane transition zone. Propane was not detected in sediments shallower than the transition zone. Below 38.40 mbsf, propane levels approach about one-third of ethane levels (Fig. F6O).

Consistent with observations from other Leg 201 sites, the 1-day headspace extraction procedure resulted in higher gas yields compared to the 20-min extraction for safety purposes (Table F3).

Hydrogen incubations were conducted on 15 samples from Hole 1227A and 6 samples from Hole 1227D (Table T4; Fig. F6P). Hydrogen concentrations are between ~0.3 and 1.2 nM, with most samples between 0.3 and 0.5 nM. Hydrogen concentrations do not change across the sulfate–methane transition zone.

A total of 58 IW samples were analyzed for ammonium, 40 from Hole 1227A and 18 from Hole 1227D. Concentrations of ammonium were below detection in the WSTP sample and at 0.6 mbsf in Hole 1227D. They reached 680 μM at 1.35 mbsf in Hole 1227A (Fig. F6Q). In both holes, ammonium concentrations steadily increase downhole, reaching 22,500 μM at the bottom of Hole 1227A (144.45 mbsf). This is

T3. Hydrocarbons in headspace, p. 61.

T4. Calculated interstitial water hydrogen, p. 62.

similar to the profile observed at Site 684 (Shipboard Scientific Party, 1988).

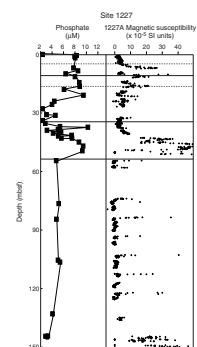
Results of phosphate analyses on 39 alkalinity samples (see “**Bio-geochemistry**,” p. 9, in the “Explanatory Notes” chapter) from Holes 1227A and 1227D (Fig. F6R) render a profile that bears little resemblance to that from Site 684 (Shipboard Scientific Party, 1988). Phosphate concentrations increase sharply in Hole 1227D, from 2.3 μM at the sediment/water interface (WSTP sample) to 8.3 μM at 0.6 mbsf, and fluctuate between 2 and 10 μM from 24 to 54 mbsf. However, a broad minimum and a broad maximum are present between 24 and 40 mbsf and 41 and 54 mbsf, respectively. Phosphate concentrations appear to maintain a fairly steady value of ~ 5 μM from 54 to 106 mbsf. Interestingly, dissolved phosphate and magnetic susceptibility exhibit somewhat similar profiles (Fig. F7).

A total of 50 samples were analyzed for dissolved silica at Site 1227, 33 from Hole 1227A and 17 from Hole 1227D. Silica correlates well with major changes in lithology (Fig. F6S). Concentrations increase rapidly from 535 μM at the sediment/water interface to between 1000 and 1100 μM from 8.4 to 13 mbsf. A dissolved silica minimum between 14 and 22 mbsf and a pronounced maximum between 40 and 55 mbsf coincide with variations in lithology from diatom-bearing ooze to the more terrigenous glauconite- and pyrite-bearing silty layers of lithostratigraphic Unit III (see “**Lithostratigraphy**,” p. 8). Thus, and in contrast to the open-ocean sites, dissolved silica concentrations are apparently lower in the diatom-bearing units. The relatively stable silica concentrations of 900 to 1000 μM maintained over the lower 90 m of the hole (lithostratigraphic Unit IV) likely reflects solubility control of IW silica by opal phases as the sediments return to predominantly diatom-rich oozes and clays.

Chloride concentrations were determined by ion chromatography. Chloride concentrations increase monotonically from 555 mM near the sediment/water interface to a maximum of 1178 mM at a depth of 164 mbsf (Fig. F6T). This trend is due to the upward diffusion of chloride from brine deeper in the sediment column. There is a slight convex-upward curvature to the profile. This curvature may result from upward advection or from decreasing diffusivity with depth. If it is assumed that diffusivity is constant, advection velocities >0.02 cm/yr would produce greater curvature than that observed.

Lithium increases downhole nearly linearly with chloride. Lithium increases by a factor of ~ 60 , whereas chloride increases by a factor of ~ 2 (Fig. F6H, F6T). This correlation provides strong evidence that the deeply buried brine is a residual solution produced during evaporite formation rather than the dissolution of evaporitic minerals, as lithium is concentrated in residual brines and excluded from halite. The extent of lithium enrichment in a brine depends on the extent of net evaporation of the original seawater. Hence, assuming no other sources or sinks for lithium, its concentration in brine can be used to calculate the extent of evaporation. As enrichment in lithium relative to chloride occurs following halite precipitation, the lithium content of the deeply buried brine can be estimated by extrapolating the lithium–chloride correlation to halite saturation. Halite saturates at ~ 6 M, which is equivalent to an approximately tenfold evaporative concentration of seawater. Using the measured lithium–chloride correlation and extrapolating to halite saturation, the inferred lithium concentration in the brine buried at Site 1227 is 0.014 M. Assuming that the lithium concentration in the initial fluid is similar to that in modern seawater, the inferred

F7. Lithostratigraphy, magnetic susceptibility, and phosphate, p. 39.



brine concentration corresponds to an evaporative concentration of a factor of ~500 during brine formation.

MICROBIOLOGY

Microbiological samples were taken from the second and fifth section of every available core between Cores 201-1227A-2H and 6H. This high-resolution microbiological sampling covered the sulfate-reducing zone and extended across the sulfate/methane interface into the methanogenic zone (see “**Biogeochemistry**,” p. 13). Beginning with Core 201-1227A-7H, every undisturbed core was sampled at a frequency of one section per core. In Hole 1227D, additional samples were obtained for microbiological and biogeochemical study from selected depths (Figs. F8, F9). The uppermost five sections of Core 201-1227D-1H were sampled to increase resolution near the sediment/water interface. Cores 201-1227D-4H, 5H, and 8H were sampled to fill any gaps remaining from our sample distribution from Hole 1227A. Higher-resolution sampling of Cores 201-1227D-4H and 5H focused on the sulfate/methane transition between 35 and 43 mbsf. Core 201-1227A-14H had a highly porous and spongy structure, presumably a result of gas-induced core expansion.

The sampling program for each section is shown in detail for Hole 1227A in Figure F8 and for Hole 1227D in Figure F9. For deoxyribonucleic acid (DNA), fluorescence in situ hybridization (FISH), adenosine triphosphate (ATP), lipid biomarker analysis, solid-phase iron/manganese/sulfur chemistry, and solid-phase phosphate chemistry, samples were fixed or frozen, as appropriate, for processing on shore (for details see “**Procedures and Protocols**,” p. 25, in “Microbiology” in the “Explanatory Notes” chapter). Whole-round cores (WRC) were subsampled into 5-mL syringes for subsequent measurements of hydrogen concentrations and for rates of tritium turnover, sulfate reduction, methanogenesis, acetate turnover, and thymidine incorporation into DNA. Samples for acridine orange direct counts were fixed from the same sections, and the cells were counted on the ship. Samples for anaerobic oxidation of methane experiments, sulfate reduction experiments, ¹⁸O isotope analysis, pyrolysis of organic material, and diffusion experiments were taken at several defined intervals (Fig. F8). Samples at ostensibly dolomite-bearing layers (Sections 201-1227A-3H-5, 8H-2, and 12H-2; confirming analysis will be done postcruise) were taken for FISH, enrichment, lipid biomarker, and sedimentological analyses. From Section 201-1227D-5H-5, where a barium peak was observed in the interstitial water profile from Hole 1227A (see “**Biogeochemistry**,” p. 13), extra samples were obtained for shore-based sulfate reduction experimentation (using radiolabeled Ba³⁵SO₄), DNA analysis, and shore-based microscopic studies and enrichment cultures on barite.

Samples for cultivation were taken from the near-surface sediment column (Sections 201-1227D-1H-1 and 201-1227A-2H-5 and 3H-5), from intermediate depths near the sulfate–methane transition (Sections 201-1227A-5H-5, 201-1227D-4H-6, and 201-1227A-7H-2), and from the deeper methanogenic portion of Hole 1227A (Sections 12H-2 and 18H-2). In order to study the role of sulfate as a biologically limiting factor, sulfate-free and sulfate-containing media were used in samples from intervals with and without sulfate.

F8. Subsampling for MBIO sections, Hole 1227A, p. 40.

F9. Subsampling for MBIO sections, Hole 1227D, p. 41.

Total Bacterial Enumeration

Samples of 1-cm³ plugs for total prokaryotic enumeration were taken on the catwalk from a total of 21 depths between 8.4 and 144.3 mbsf in Hole 1227A (15 samples) and between 0.15 and 38.8 mbsf in Hole 1227D (6 samples). Additionally, 2-mL samples of 25% slurry (vol/vol) were taken from six slurries prepared in the laboratory (see “**Preparation of Slurries**,” p. 28, in “Procedures and Protocols” in “Microbiology” in the “Explanatory Notes” chapter). Prokaryotic cells were present in all enumerated samples taken from the catwalk to 144.3 mbsf (Fig. F10). The highest number of prokaryotes was found in the near-surface sample (Sample 201-1227D-1H-1, 15–16 cm), which contained 1.42×10^7 cells/cm³. The lowest number of prokaryotes was at the base of the hole, with 1.77×10^6 cells/cm³, an eightfold decrease.

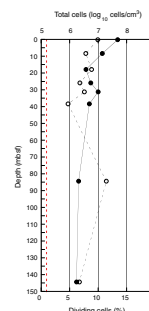
The overall depth profile of cell numbers per cubic centimeter follows a trend observed at other ODP sites (Parkes et al., 1994). However, cell numbers are persistently lower than the average from previous sites (Fig. F11). All data except the shallowest sample depth fit within the 2- σ envelope around the fit of total censused data from previous ODP sites. Counting has so far focused on the sulfate–methane transition zone, between ~35 and 43 mbsf (see “**Biogeochemistry**,” p. 13). Cell numbers were maximal at 31.3 mbsf (Sample 201-1227A-4H-5, 105–110 cm), with 1×10^7 cells/cm³ (Fig. F10). Two-sample t-tests established that the numbers of prokaryotes at this depth were significantly greater than those from the sample directly above ($t = 3.91$; $n = 6$; $P < 0.05$) at 25.95 mbsf (Sample 201-1227A-4H-1, 135–140 cm) and from the sample directly below ($t = 5.18$; $n = 6$; $P < 0.01$) at 38.4 mbsf (Sample 5H-3, 130–135 cm).

Numbers of dividing cells (suggested as an index of growth activity) are typically <10% of the total count. As expected, dividing cells, as a percentage of the total count, are high near the surface (Fig. F10) and then decrease steadily to a minimum at 38.4 mbsf (Sample 201-1227A-5H-3, 130–135 cm). The two data points below this depth suggest that dividing cells increase at greater depth; however, there are insufficient data here to justify any conclusions. The high amount of organic matter in the sediment at this site made direct counting more problematic than usual. Where subsamples of 15–40 μ L can generally be processed, in this case, subsample size was restricted to a maximum of 12 μ L. Consequently, the detection limit increased to 1.3×10^5 cells/cm³ (Fig. F10) and thus counting sensitivity decreased.

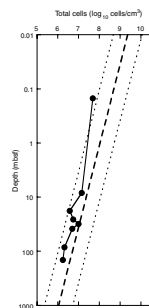
Contamination Tests

While drilling cores for microbiology, the potential for contamination with bacteria from the surface is highly critical. Contamination tests were continuously conducted using solutes (perfluorocarbon tracer [PFT]) or bacterial-sized particles (fluorescent microspheres) to check for the potential intrusion of drill water from the periphery toward the center of cores and thus to confirm the suitability of the core material for microbiological research. We used the chemical and particle tracer techniques described in ODP *Technical Note 28* (Smith et al., 2000). Furthermore, the freshly collected cores were visually examined for possible cracks and other signs of disturbance by observation through the transparent core liner. Core sections observed to be disturbed before or after subsampling were not analyzed further. Such dis-

F10. Prokaryotic cells enumerated, p. 42.



F11. Total prokaryote profile, p. 43.



turbance phenomena are critical to the integrity of the core material and therefore also to its usefulness for microbiological studies.

Perfluorocarbon Tracer

The perfluorocarbon tracer (PFT) was injected continuously into the drilling fluid during drilling of Holes 1227A and 1227D (see “**Perfluorocarbon Tracer Contamination Tests**,” p. 26, in “Procedures and Protocols” in “Microbiology” in the “Explanatory Notes” chapter). PFT sampling focused on microbiology cores and especially on sections that were used for slurry preparation and cultivations. To increase the sensitivity of PFT detection, two (instead of one) 5-cm³ subcores were taken from the center of a section and pooled for PFT measurement at Site 1227. This strategy was used at all further sites of Leg 201. The increased amount of sample material resulted in an improved detection of PFT (corresponding to ~0.01 µL seawater contamination/g sediment), under the reasonable assumption that the PFT signal follows proportionally the twofold increased sample volume. In parallel, samples were taken from the outer portion of each sediment core next to the core liner to assess the difference in contamination potential between inner and outer portions of a core. Whenever possible, the samples were taken directly on the catwalk because the PFT content of catwalk air was usually not detectable.

Low levels of potential seawater contamination (Table T5) were found for the center portions of all tested cores of Holes 1227A and 1227D and did not exceed 0.05 µL seawater/g sediment (average = 0.021 µL seawater/g sediment). The outer portions of all tested cores had a significantly higher level of PFT tracer and potential seawater contamination (average = 1.77 µL seawater/g sediment). In all cases, the PFT content and the estimated potential seawater contamination levels were higher at the periphery of the core than in the center. Two samples showed seawater contamination levels of more than double the average from Sections 201-1227A-7H-2 and 201-1227D-4H-6, indicating high variability and patchiness for the more highly contaminated areas in the outer core.

Of the six master slurry samples taken from Site 1227 (Table T6), only the slurry from Core 201-1227A-3H showed small concentrations of PFT (~0.03 µL potential seawater contamination/g slurry). This value is near the detection limit of 0.025 µL potential seawater contamination/mL slurry. Assuming 5×10^8 prokaryotic cells/L surface seawater, each 0.1 µL seawater contamination may represent as many as 50 contaminating cells if the sediment is porous enough to allow cells to travel with the PFT.

Particulate Tracer

Fluorescent beads were deployed on seven occasions at this site, including all cores from which slurries were made. On two occasions the bead bag failed to burst. The first time this happened (Core 201-1227A-5H), it remained unrecognized until well after slurry processing had finished. At the second occurrence, the failure was recognized immediately and beads were run on the following core, and the slurry was made on the latter core (Section 201-1227A-12H-2). Modifications to the delivery mechanism for bead bags were made at the next site. For each slurry, the presence of beads was checked in up to three subsamples: (1) a sample of the slurry; (2) when necessary, a sediment sample

T5. Seawater contamination based on PFT, p. 63.

T6. Potential contamination of slurries based on PFT, p. 64.

tenfold diluted in 2% formaldehyde (used also for direct prokaryotic counts); and (3) a scraping from the outer surface of the core (processed to confirm deployment of beads). Beads were not detected in any of the six slurries. The presence of beads was confirmed from the outer core scrapings in all slurries (not in Core 201-1227A-5H), confirming deployment. Consistent with the low PFT values, no beads were detected in any of the slurries from Site 1227.

Cultivations

Vertical profiling of geochemical parameters indicated that the sulfate–methane transition is present from 35 to 43 mbsf (see Fig. F6). Accordingly, the presence of prokaryotes possibly responsible for sulfate reduction, acetogenesis, and methanogenesis throughout the sulfate–methane transition were evaluated by a combined approach of enrichment cultures and most probable number assays. Samples for slurries were taken from five different depths in Hole 1227A, including the sulfate–methane transition zone, and from two samples in Hole 1227D (Table T7). The slurry samples were taken by subcoring with two 60-mL syringes from the center of two freshly broken sediment core surfaces. The slurry was used to inoculate media for growing sulfate reducers, methanogens, and various anaerobic chemolithoautotrophic and heterotrophic microorganisms that could use iron(III), manganese(IV), chlorate, or nitrate as an electron acceptor. To use larger sample volumes for inoculations and to avoid the dilution that a sediment sample undergoes during slurry preparation, core material freshly harvested with 5- and 60-mL syringes was also used directly for inoculations. All shipboard cultivation experiments and their media and incubation temperatures are shown in Table T7. In order to study the influence of sulfate as a limiting factor on the deep biosphere, both sulfate-free and sulfate-containing media were used for inoculation of samples from the sulfate-containing layers, the sulfate–methane transition zone, and sulfate-free layers. For details of the various media compositions and incubation conditions see “**Procedures and Protocols**,” p. 25, in “**Microbiology**” and Tables T4, p. 84, T5, p. 85, and T7, p. 88, all in the “**Explanatory Notes**” chapter.

T7. Media inoculated with material from Site 1227, p. 65.

FISH-SIMS

¹³C substrate incubations were initiated for postcruise analysis by FISH-secondary ion mass spectrometry (SIMS) using material from Cores 201-1227A-3H and 5H and 201-1227D-4H. In this case, 10 mL of the master slurry was injected into each bottle. The ¹³C substrates used were methane, acetate, and glucose. For Cores 201-1227A-3H and 5H, one of each bottle was inoculated. For Core 201-1227D-4H, two bottles with each substrate and two ¹³C acetate bottles containing nonlabeled methane in the headspace were inoculated.

PHYSICAL PROPERTIES

At Site 1227 we collected a full range of physical property data from the sediment/water interface to the limit of coring at 151.1 mbsf. The data are described below and compared with those from Site 684 (Shipboard Scientific Party, 1988). Higher-resolution sampling than that used at Site 684 was feasible with current laboratory instruments.

Whole-round cores were degassed for up to 2 hr on the catwalk when necessary for safety, were equilibrated to laboratory temperature (2–4 hr), and then each available section was run on the multisensor track (MST). The standard MST measurements were magnetic susceptibility (spacing = 5 cm, data acquisition scheme [DAQ] = 2×1 s), GRA bulk density (spacing = 10 cm, count time = 5 s), *P*-wave velocity (spacing = 10 cm, DAQ = 10), and NGR (spacing = 30 cm, count time = 15 s). Thermal conductivity measurements were made on the third section of each whole-round core in Hole 1227A, where possible. Physical properties were measured on the microbiology sections only if intact parts remained following the sampling. This greatly limited the continuity and, hence, spatial resolution of the physical property record below ~30 mbsf. Hole 1227B was logged at higher resolution and precision on the MST, whereas Holes 1227C, 1227D, and 1227E were logged at the same rates as Hole 1227A.

Moisture and density (MAD) properties, *P*-wave velocity from the digital velocimeter, and resistance data (translated to formation factor, as detailed in “**Formation Factor**,” p. 47, in “Physical Properties” in the “Explanatory Notes” chapter) were collected regularly only from Hole 1227A because of MAD processing time constraints. MAD samples were taken at a frequency of one sample per section and at higher resolution in sections with many voids or lithologic transition areas. Where possible, MAD samples were co-located with the methane headspace extractions to facilitate the volumetric analysis of methane concentrations. Spot sampling for MAD was also carried out in Hole 1227D in order to confirm measurements from Hole 1227A. Even though core recovery decreased significantly below ~52 mbsf, the collected data are sufficient to allow characterization of the physical parameters of each lithostratigraphic unit and to be confident of the correspondence of our data to those from Site 684.

Instrumentation, measurement principles, and data transformations are further discussed in “**Physical Properties**,” p. 41, in the “Explanatory Notes” chapter.

Infrared Scanner

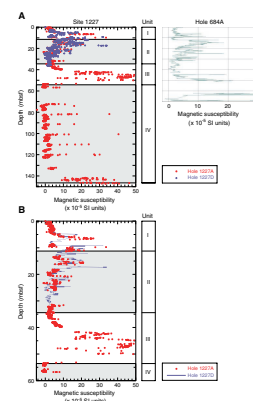
The infrared scanner was not employed at this site, due to expected rapid recovery and high concentrations of hydrogen sulfide that created safety concerns.

Magnetic Susceptibility

Low-field volume magnetic susceptibility was measured on the MST using the Bartington loop sensor as described in “**Magnetic Susceptibility**,” p. 44, in “MST Measurements” in “Physical Properties” in the “Explanatory Notes” chapter. Leg 112 magnetic susceptibility data are not available in digital format. However, a visual comparison between our data and the postcruise records collected for Sites 684 (Fig. F12A) (Merrill et al., 1990) shows a reasonable match across the uppermost 70 mbsf, where the records are most continuous.

Lithostratigraphic Units I, II, and III comprise a series of laminated to partly bioturbated biogenic oozes, interstratified with unconsolidated mixed detrital and biogenic silts and sands (see “**Description of Lithostratigraphic Units**,” p. 9, in “Lithostratigraphy”). The oozes are typified by relatively low magnetic susceptibilities in the range of 1×10^{-5} to 5×10^{-5} SI units. The coarser-grained layers are associated with mag-

F12. Comparison of magnetic susceptibility data, p. 44.



netic susceptibility peaks that range from 25×10^{-5} to 50×10^{-5} SI units. The most prominent of these layers are located between 5 and 7 mbsf (Unit I), 9 and 12 mbsf (Unit I/II boundary), 14 and 18 mbsf (Unit II), and 41 and 53 mbsf (Unit III) (Fig. F12B).

These peaks in the susceptibility signal, coincident with grain size and NGR increases, are probably the result of a change in the origin of the sediment. Using a permanent (Nd) magnet, extracts from dried samples and slurries were obtained from the layers at 5–7, 9–12, and 41–53 mbsf for optical and XRD analysis. Preliminary studies suggest the source of the magnetism is primary magnetite. Rounding and size of the extracted crystals suggest they have been transported rather than formed in situ by diagenetic or microbial processes.

The magnetic susceptibility record in the lower part of Hole 1227A is incomplete. Most of the intact parts of cores are composed of recovery-induced gas-fractured oozes that have a very low magnetic susceptibility signature. Magnetic susceptibility spikes appear at the top of each core below ~60 mbsf (Section 201-1227A-7H-3), the depth at which we encountered a high-susceptibility sand and calcite-cemented unit. This material apparently fell down the hole after each successive core and was therefore present at the top of each core as a drilling artifact. The possible exception is the peak at ~110 mbsf, which appears to be associated with an in situ coarser-grained layer.

Paleomagnetism

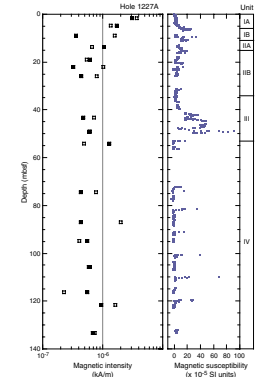
At Site 1227 we collected 18 discrete samples for paleomagnetic measurements. The sampling frequency was two samples from each core in Cores 201-1227A-1H through 3H (0.0–24.6 mbsf) and one sample from each core below this interval to the bottom of the hole (Cores 201-1227A-4H through 17H; 24.6–141.6 mbsf). Alternating-field (AF) demagnetization of the natural remanent magnetization (NRM) was conducted up to 40 mT in 10- or 5-mT steps. Anhyseretic remanent magnetization (ARM) was measured to 40 mT in 10-mT steps with a 29- μ T direct current-biasing field. AF demagnetization of the ARM was conducted to 40 mT in 10-mT steps.

Diatomaceous and siliciclastic sediments at Site 1227 show low magnetic intensity and susceptibility (Fig. F13) compared with the other sites occupied during Leg 201. The uppermost dark brown clay-rich diatom ooze sample (Sample 201-1227-1H-2, 14–16 cm) shows a less stable magnetic direction (Fig. F14). Although samples from lithostratigraphic Unit II (see “Description of Lithostratigraphic Units,” p. 9, in “Lithostratigraphy”) exhibit higher susceptibility, we were not able to isolate a clear magnetic signal.

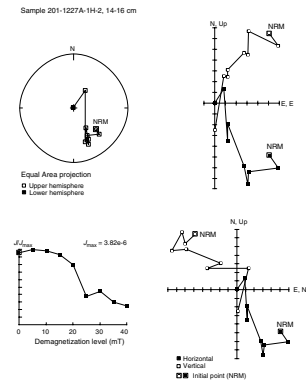
Density and Porosity

Density data were measured on the MST by the GRA densitometer (spacing = 10 cm, count time = 5 s) and calculated from split-core mass/volume (MAD) measurements. The GRA data from Site 1227 show much less scatter than the Site 684 data (Shipboard Scientific Party, 1988) (Fig. F15) and are consistently at the high end of the values for Site 684, though the trends in the two data sets are nearly identical. Figure F16 displays a 5-m moving average of the GRA density estimates from Holes 1227A and 684C, showing that the two surveys have good correlation until ~30 mbsf. Below this depth, the continuity of both records decreases because of poor core recovery.

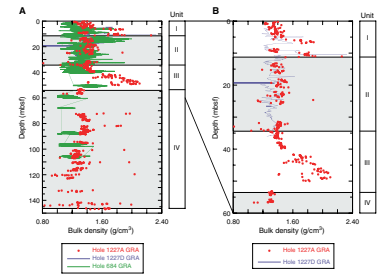
F13. Magnetic intensity and susceptibility, p. 45.



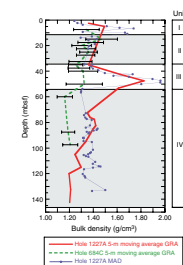
F14. Principal component analysis of NRM, p. 46.



F15. Comparison of GRA density, p. 47.



F16. Comparison of GRA and MAD density, p. 48.



GRA density is generally between 1.2 and 1.4 g/cm³ throughout the profile. As with magnetic susceptibility, there are several intervals where density peaks. The density increases to ~2.0 g/cm³ at 5–7, 9–11, and 42–53 mbsf (Fig. F15B). These peaks correlate with a coarse-grained foraminifer ooze located at the base of Unit I, a foraminifer-enriched silt at the Unit I/II boundary, and a glauconitic silt comprising Unit III. There also appears to be an increase in bulk density from 140 mbsf to the bottom of the hole, but the record is noisy and the trend may be an artifact of coring.

Between 50 and 125 mbsf, the MAD-calculated density increases slightly from ~1.2 to ~1.4 g/cm³ (Figs. F16, F17A). This compaction-related trend is not reflected in the GRA data, which show a bulk density decrease that is attributed to unfilled core liner effects and decompression/degassing disturbance.

Porosity data derived from the MAD measurements (Fig. F17C) indicate an initial porosity for fine-grained sediment of ~85% at the seafloor. This declines to ~70% for the deepest measurement at ~140 mbsf. The coarser-grained units described above have distinctly lower porosities, consistent with the more equant grain shapes and framework support of the fabric. The uppermost silts in Unit I have porosities of ~60%, whereas the thicker silt layer in Unit III has a porosity of <50%.

Grain density data (Fig. F17B) support the mineral identifications discussed in “Lithostratigraphy,” p. 8. Grain densities of ~2.8 g/cm³ are consistent for coarse-grained silts, compared with values of 2.2 to 2.4 g/cm³ for the finer-grained sediments that dominate Units II and IV (Carmichael, 1982).

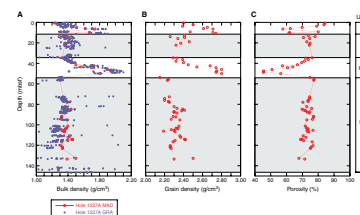
Compressional Wave Velocity

P-wave data from the MST *P*-wave logger (PWL) were recorded (spacing = 10 cm, DAQ = 10) for all APC cores from Holes 1227A to 1227E and at 2-cm spacing for Hole 1227B. The PWS3 velocimeter was also used to measure *P*-wave velocities on split cores from Hole 1227A, with measurements taken at a minimum of one per section (depending on lithologic boundaries) for Sections 201-1227A-1H-1 through 5H-6. Below Section 201-1227A-5H-6 (43.1 mbsf), reliable PWL and PWS3 measurements were unobtainable because of decompression and drainage effects, which created partially saturated cracklike voids of ~2–10 mm length oriented perpendicular to the core axis.

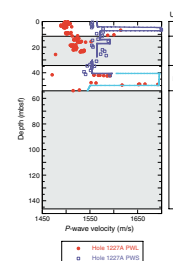
Between 0 and 55 mbsf, PWL measurements range from 1485 to 1695 m/s, whereas PWS3 velocities are bounded within 1540–1700 m/s (Fig. F18). The PWS measurements were generally 40–50 m/s faster (similar to measurement differences at Site 1226). The breakdown of PWS velocities based on lithostratigraphic units is as follows: Unit I (diatom ooze) ranges from 1550 to 1570 m/s; Unit II (diatom-bearing clay- and pyrite-rich silt) ranges from 1550 to 1580 m/s; and Unit III (glauconite-bearing pyrite-rich silt) ranges from 1535 to 1560 m/s. Based on several measurement sets of 10-cm-spaced velocity profiles over ~1.5 m, the 20- to 30-m/s velocity variation within the respective units represents natural meter-scale variability and is not indicative of a particular sedimentary sequence.

Three high-velocity intervals (beginning at 6.2, ~14.0, and ~42.0 mbsf, respectively) (Fig. F18) correlate with coarse-grained foraminifer ooze (Unit I), foraminifer-enriched silt (Unit II), and glauconitic silt (Unit III). The velocities in these intervals are at least 1700 m/s, which

F17. MAD measurements, p. 49.



F18. *P*-wave velocity profiles, p. 50.



we consider to be an in situ minimum because of the unconsolidated nature of these sediments in split cores.

Natural Gamma Ray Emission

NGR was measured on the MST for all Site 1227 holes (spacing = 30 cm, count time = 15 s). Hole 1227B was run at a higher spatial resolution (spacing = 15 cm, count time = 15 s). As with other physical properties at this site, the NGR data (Fig. F19) track the compositional anomalies in the layers located between 5 and 7 mbsf (Unit I), 9 and 12 mbsf (Unit I/II boundary), 14 and 18 mbsf (Unit II), and 41 and 53 mbsf (Unit III). The higher emission signal in these layers is probably linked to the presence of feldspars and glauconite (see “Description of Lithostratigraphic Units,” p. 9, in “Lithostratigraphy”).

Thermal Conductivity

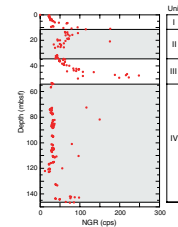
Thermal conductivity measurements were made on Hole 1227A sediments at a rate of one per core (usually the third section, at 75 cm, if this was available). Values range between 0.70 and 0.94 W/(m·K) (average = 0.76 W/[m·K]). The maximum thermal conductivity is at 47.0 mbsf. This corresponds to the glauconitic silt in Unit III, the interval of lowest downhole porosity. Average normalized thermal conductivity and bulk density show a high correlation (Fig. F20), indicating that the thermal conductivity is an inverse function of water content of the sediments. Thermal conductivity measurement quality decreased for Core 201-1227A-13H and below, due to unfilled core liners and drilling disturbance.

Formation Factor

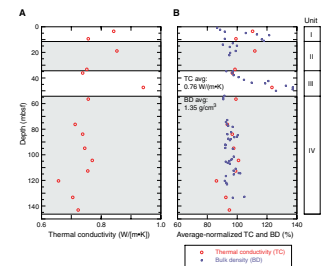
Formation factor (longitudinal and transverse) was determined for Hole 1227A sediments as described in “Formation Factor,” p. 47, in “Physical Properties” in the “Explanatory Notes” chapter, with a minimum of one sample per section for Cores 201-1227A-1H through 17H. Measurements in all cores below Core 201-1227A-12H (beginning at ~110 mbsf) were made after saturating pilot holes in the split core face with seawater before inserting the four-pin probe, to account for decompression voids and water content decrease resulting from extended air exposure after splitting (hydrogen sulfide degassing precaution). Data reported herein correspond to high-quality measurements taken in minimally disturbed APC intervals.

Longitudinal (parallel to core axis) formation factors range from 1.5 to 2.9 except in the coarser-grained intervals at 6.2 and 41.0 mbsf, where measurements make steplike increases to >4.5 (Fig. F21). The low values below ~116 mbsf are probably decompression artifacts, as the sediment framework shows consistent expansion features that would tend to make electrical conductivity pathways less tortuous than in situ conditions. Electrical conductivity anisotropy typically ranges from 3% to 15% (average = 7%). Overall, the formation factor measurements track the changing lithostratigraphy, delineating the sharp grain-size and component-mix changes in Units I and III.

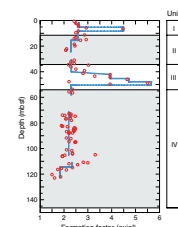
F19. NGR profile, p. 51.



F20. Thermal conductivity measurements, p. 52.



F21. Formation factor profile, p. 53.



Summary and Discussion

The physical properties of the units at Site 1227 are due to the dramatic compositional variation between the coarser and finer sediments and the variable impact of burial on the different sediments. The coarser layers have diagenetic pyrite and are in a foraminifer matrix. In Unit I, the coarser layers comprise a mixture of clastic grains, primarily quartz, and hornblende. Unit III has redeposited shallow-water glauconitic grains. High magnetic susceptibility, high bulk density, high *P*-wave velocity, high formation factor, low porosity, and high natural gamma radiation characterize these layers. The coincidence of high bulk density and low porosity can be explained by the composition of the material and the compactional history of the sand and silt compared with the ooze. The NGR response most likely arises from decay of potassium in the feldspars and glauconite.

The finer sediments are primarily diatomaceous oozes. The ooze has characteristic low NGR values and shows slightly increasing density and decreasing porosity downhole. These are the expected trends as a result of compaction.

DOWNHOLE TOOLS

Six downhole tools were employed at Site 1227: the Adara temperature shoe, the DVTP, the DVTP-P, the WSTP, the APC-M, and the PCS. The results of the temperature and pressure measurements at Site 1227 are described in the first two sections below. Results of other tools are briefly mentioned in the last section.

In Situ Temperature Measurements

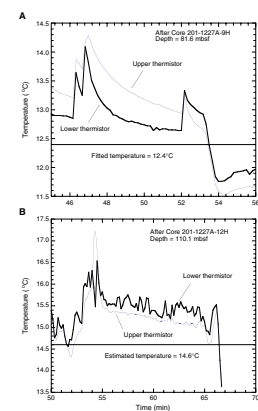
Five determinations of temperature were made at Site 1227 using the Adara APC temperature tool, the DVTP, and the WSTP. All three of the downhole temperature records were either of poor quality or deviated from the values expected from the Leg 112, Site 684 data. Table T8 summarizes the deployments and the observed problems. Figure F22 shows the data from the two DVTP deployments at 81.6 and 110.1 mbsf. Both records show considerable small-scale oscillations and double peaks when the tool is first pushed into the sediments. The record from 81.6 mbsf (after Core 201-1227A-9H) lasts for only 5 min before the temperature jumps up and again decays for the remainder of the 10-min deployment. The record for the lower thermistor from 110.1 mbsf (after Core 201-1227A-12H) is too noisy to be fit and provides only an upper bound on in situ temperature.

The results of the DVTP temperature estimates are displayed in Figure F22. In situ temperatures were estimated by extrapolation of the station data using thermal conductivities measured on adjacent cores to correct for the frictional heating on penetration as described in “Downhole Tools,” p. 49, in the “Explanatory Notes” chapter. Because of the overall poor quality of the Site 1227 downhole temperature data, the results from Site 684 are given in the summary table and were included in the thermal gradient estimate.

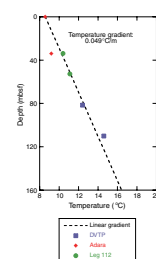
The combined in situ temperatures of Sites 1227 and 684 define a gradient of 0.0492°C/m in the upper 110 m of the sediment column (Fig. F23). Extrapolating the temperatures using this gradient yields a value of 16.4°C at the bottom of Hole 1227A (160 mbsf). Multiplying

T8. Temperature measurements, p. 66.

F22. DVTP temperature records, p. 54.



F23. Temperatures vs. depth, p. 55.



the gradient by an average thermal conductivity of 0.76 W/(m·K) (Fig. F20A) yields a conductive heat flow estimate of 37.3 mW/m² at Site 1227. This result is slightly higher than the value of 31 mW/m² obtained for Site 684 by the Leg 112 Shipboard Scientific Party (1988).

Comparing lithology from locations that produced good and bad temperature decay profiles showed some differences that may be used to optimize future DVTP deployments. The better DVTP deployment at 81.6 mbsf occurred between cores composed of clay and nannofossil-bearing diatom ooze (Cores 201-1227A-9H and 10H). These fine-grained sediments are similar to those from Site 1225 and 1226, where the acquired temperature data were excellent. In contrast, the second deployment location at 100.1 mbsf occurred between cores of pyrite and diatom-rich silty clays with sand-sized particles (Cores 201-1227A-12H and 13H). These sediments were significantly more coarse grained than those cored from above and below the better deployment (see “Density and Porosity,” p. 23, in “Physical Properties”). Accumulation of gravel in the base of the hole does not appear to differ between the two deployments. Both locations had ~40 cm of gravel at the top of the subsequent core. Another aspect of Site 1227 that may be important is the shallow 423-m water depth compared to >3000 m at Sites 1225 and 1226. The increased noise in the data may be due to the greater influence of heave or currents on the tool in shallow water. It appears that for deployments in shallow water the best strategy may be to choose fine-grained intervals for the deployments.

Davis-Villinger Temperature-Pressure Probe

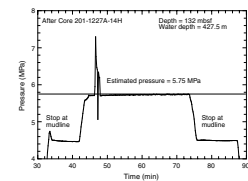
The DVTP-P was deployed once at Site 1227 at a depth of 132 mbsf (after Core 201-1227A-14H). The record displayed in Figure F24 shows a relatively noise-free signal with the expected sharp pressure increase when the tool was pushed into the sediments. Within 2 min, the pressure dropped to the value initially recorded at the base of the hole. A pressure signal equivalent to in situ hydrostatic pressure with relatively little noise was recorded during the remainder of the 30-min deployment. The rapid return to hydrostatic pressure suggests that the sealing of the formation around the tool was poor. The abrupt drop in pressure for one data value after 40 s is probably due to suction when the tool is pulled upward by heave of the drill string.

Other Tools

A sample of bottom water was collected with the WSTP at 10 m above the seafloor. Quality assessed using a lithium tracer indicated only 4% dilution of the bottom-water sample by the water in the sampling tube. The APC-M tool was deployed in Hole 1227A continuously from Cores 201-1227A-4H through 5H and in Hole 1227D continuously from Cores 201-1227D-1H through 7H. The recovered data from this run showed that the tool and data logger functioned correctly. The data from the APC-M tool will be analyzed postcruise.

Both the PCS and FPC tools were deployed between 128 and 132 mbsf, but neither run was successful. The PCS core never closed. The FPC tool only recovered a handful of pebbles and shell hash.

F24. DVTP-P pressure record, p. 56.



REFERENCES

- Berggren, W.A., Hilgen, F.J., Langereis, C.G., Kent, D.V., Obradovich, J.D., Raffi, I., Raymo, M.E., and Shackleton, N.J., 1995a. Late Neogene chronology: new perspectives in high-resolution stratigraphy. *Geol. Soc. Am. Bull.*, 107:1272–1287.
- Berggren, W.A., Kent, D.V., Swisher, C.C., III, and Aubry, M.-P., 1995b. A revised Cenozoic geochronology and chronostratigraphy. In Berggren, W.A., Kent, D.V., Aubry, M.-P., and Hardenbol, J. (Eds.), *Geochronology, Time Scales and Global Stratigraphic Correlation*. Spec. Publ.—SEPM (Soc. Sediment. Geol.), 54:129–212.
- Carmichael, R.S., 1982, *Handbook of Physical Properties of Rock*, Vol. 3: Boca Raton, FL (CRC Press).
- Dickens, G.R., 2001. Sulfate profiles and barium fronts in sediment on the Blake Ridge; present and past methane fluxes through a large gas hydrate reservoir. *Geochim. Cosmochim. Acta*, 65:529–543.
- Garrison, R.E., and Kastner, M., 1990. Phosphatic sediments and rocks recovered from the Peru margin during ODP Leg 112. In Suess, E., von Huene, R., et al., *Proc. ODP, Sci. Results*, 112: College Station, TX (Ocean Drilling Program), 111–134.
- Hoehler, T.M., Alperin, M.J., Albert, D.B., and Martens, C.S., 1998. Thermodynamic control on hydrogen concentrations in anoxic sediments. *Geochim. Cosmochim. Acta*, 62:1745–1756.
- Kastner, M., Elderfield, H., Martin, J.B., Suess, E., Kvenvolden, K.K., and Garrison, R.E., 1990. Diagenesis and interstitial-water chemistry at the Peruvian continental margin—major constituents and strontium isotopes. In Suess, E., von Huene, R., et al., *Proc. ODP, Scientific Results*, 112: College Station, TX (Ocean Drilling Program), 413–440.
- Merrill, D.L., Ohnstad, T., and McCabe, R., 1990. Magnetic susceptibility measurements of Leg 112 cores. In Suess, E., von Huene, R., et al., *Proc. ODP, Sci. Results*, 112: College Station, TX (Ocean Drilling Program), 677–683.
- Parkes, R.J., Cragg, B.A., Bale, S.J., Getliff, J.M., Goodman, K., Rochelle, P.A., Fry, J.C., Weightman, A.J., and Harvey, S.M., 1994. A deep bacterial biosphere in Pacific Ocean sediments. *Nature*, 371:410–413.
- Paull, C.K., Matsumoto, R., Wallace, P.J., and Dillon, W.P. (Eds.), 2000. *Proc. ODP, Sci. Results*, 164: College Station, TX (Ocean Drilling Program).
- Shipboard Scientific Party, 1988. Site 684. In Suess, E., von Huene, R., et al., *Proc. ODP, Init. Repts.*, 112: College Station, TX (Ocean Drilling Program), 525–596.
- , 1992a. Site 846. In Mayer, L., Pisias, N., Janecek, T., et al., *Proc. ODP, Init. Repts.*, 138 (Pt. 1): College Station, TX (Ocean Drilling Program), 265–333.
- , 1992b. Site 851. In Mayer, L., Pisias, N., Janecek, T., et al., *Proc. ODP, Init. Repts.*, 138 (Pt. 2): College Station, TX (Ocean Drilling Program), 891–965.
- Smith, D.C., Spivack, A.J., Fisk, M.R., Haveman, S.A., Staudigel, H., and ODP Leg 185 Shipboard Scientific Party, 2000. Methods for quantifying potential microbial contamination during deep ocean coring. *ODP Tech. Note*, 28 [Online]. Available from the World Wide Web: <<http://www-odp.tamu.edu/publications/tnotes/tn28/INDEX.HTM>>. [2002-03-30]
- Suess, E., von Huene, R., et al., 1988. *Proc. ODP, Init. Repts.*, 112: College Station, TX (Ocean Drilling Program).

Figure F1. Track line for 3.5-kHz survey in the vicinity of Site 1227. Time points are in Universal Time Coordinated, contours are fit to precision depth recorder measurements, and the extent of sediment patches are estimated from crossing lines.

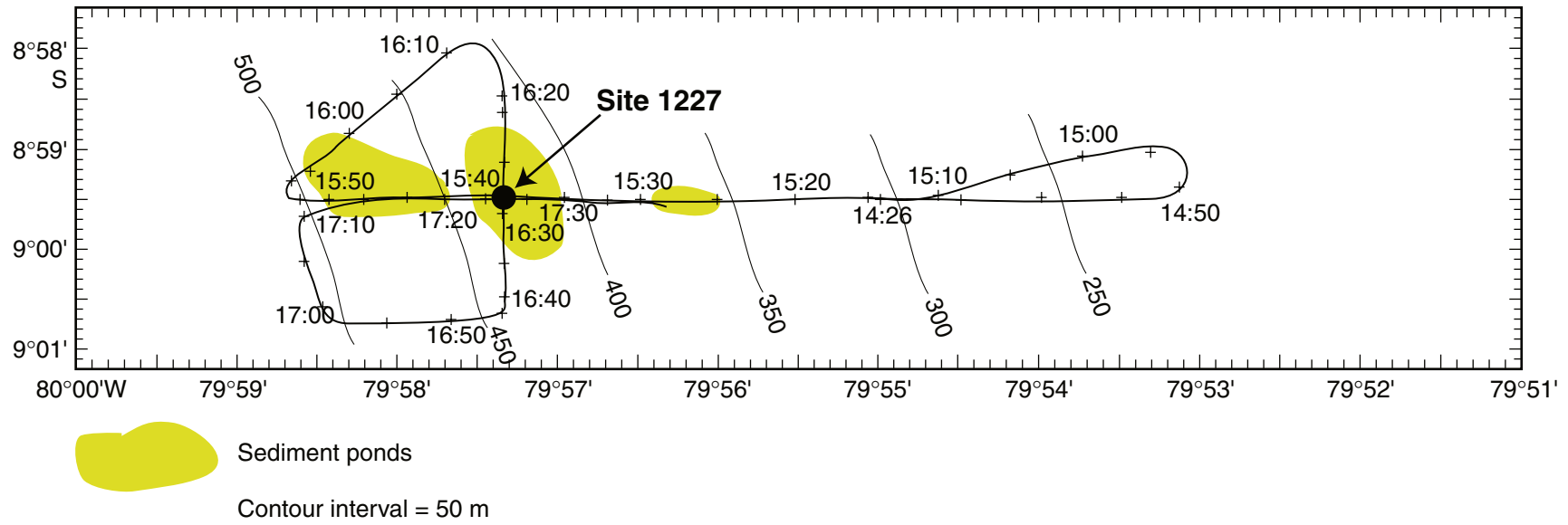


Figure F2. Lithostratigraphic summary for Site 1227. TD = total depth.

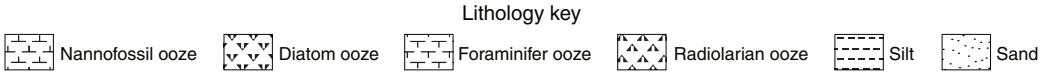
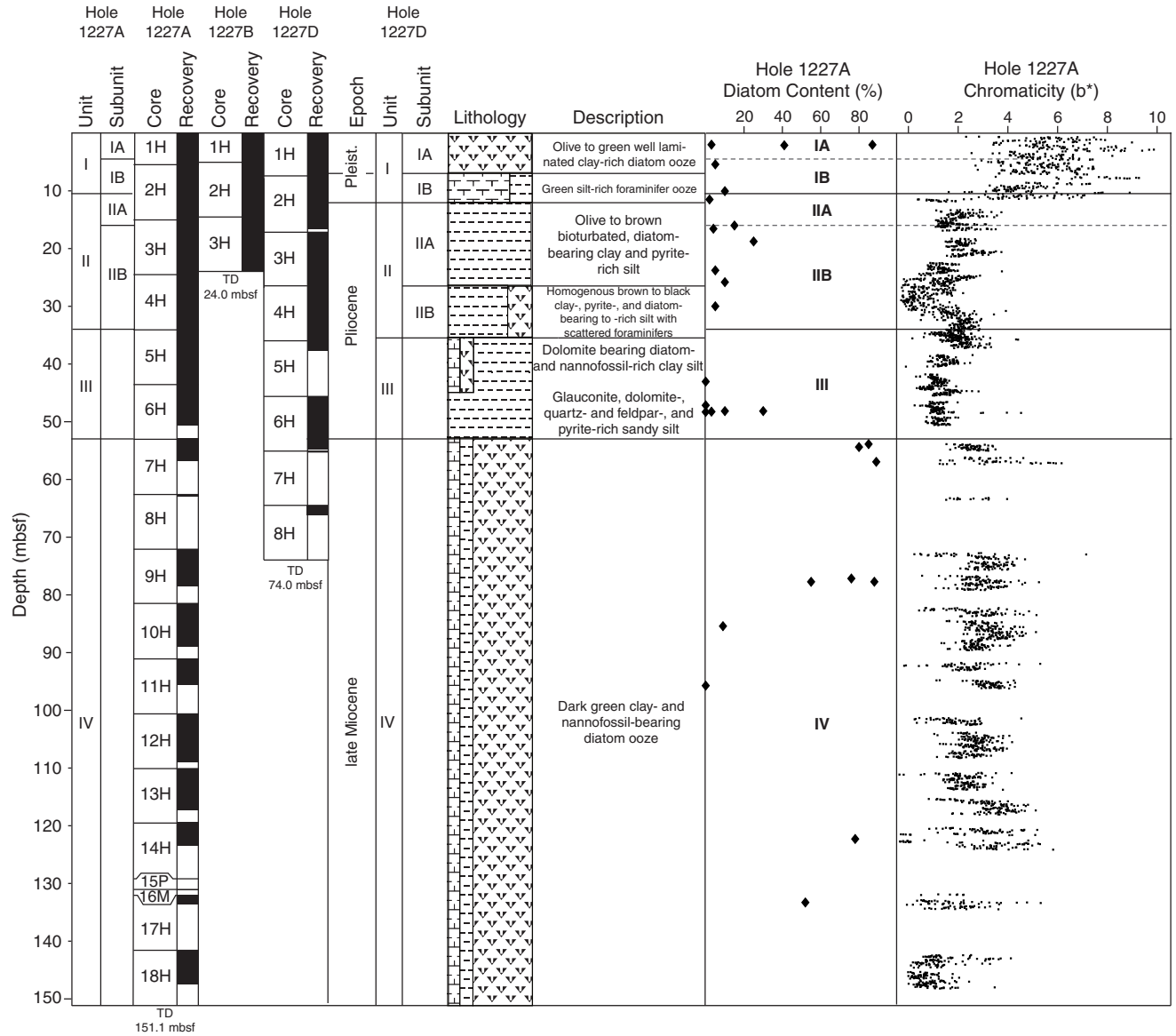


Figure F3. Lithostratigraphic summary for Site 1227 plotted together with magnetic susceptibility and natural gamma radiation variations from Hole 1227A. TD = total depth.

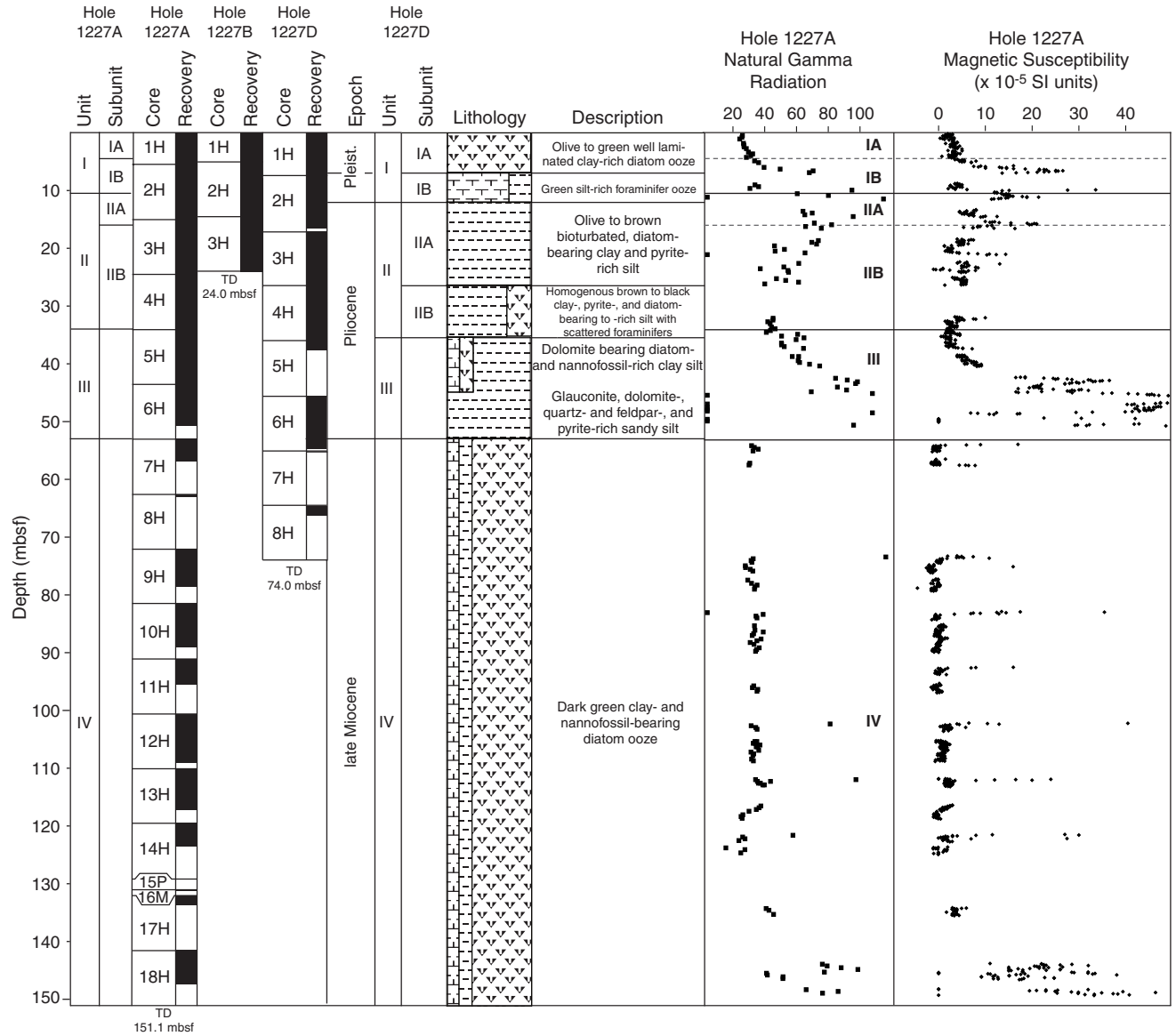


Figure F4. Close-up photos. A. Fine-scale lamination in the diatom ooze of Subunit IA. B. Coarse-grained foraminifer ooze. (Continued on next page.)



Figure F4 (continued). C. Bone fragment in Subunit IB. D. Black massive phosphate nodule from Subunit IIA. E. White barite veins.

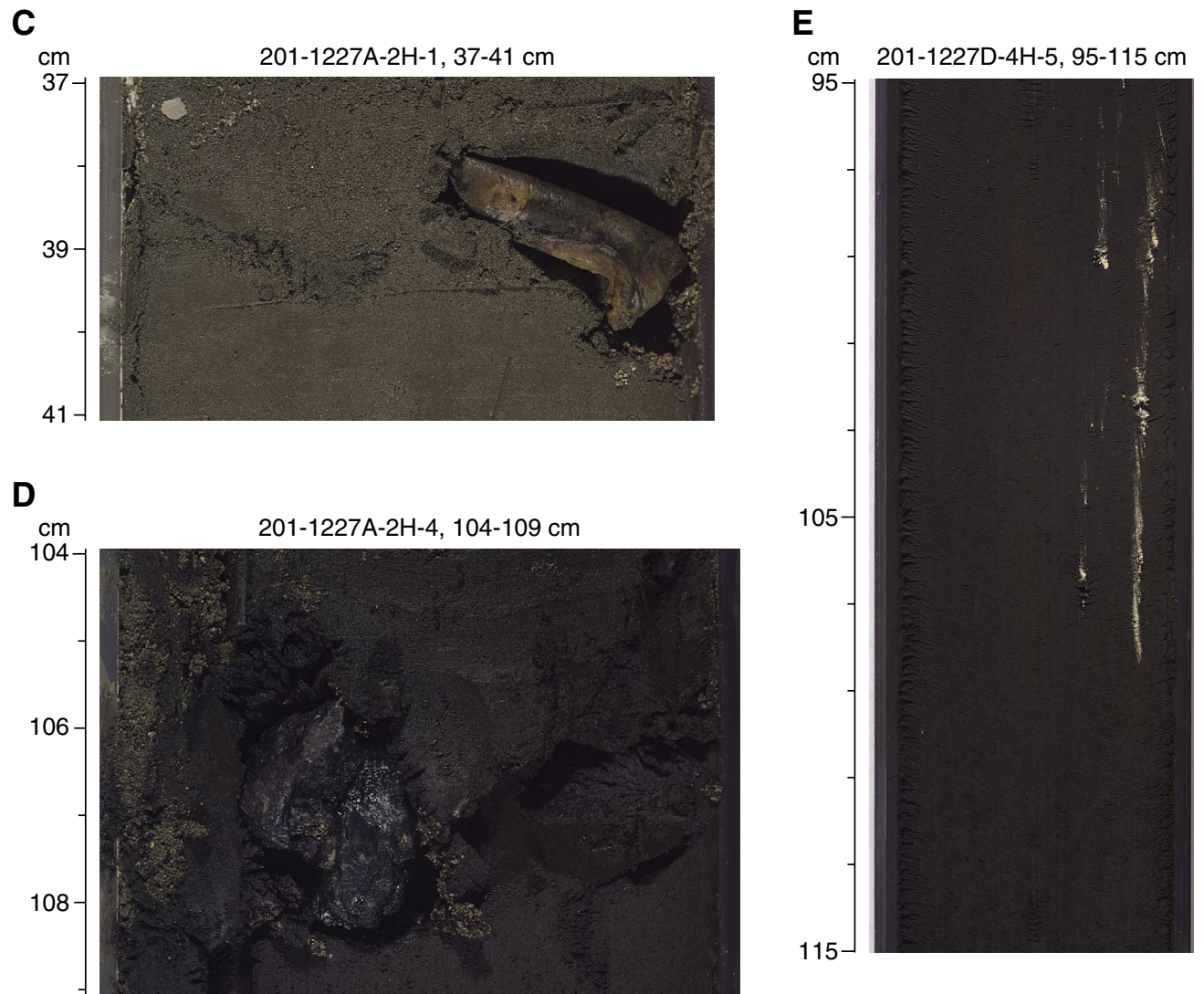


Figure F5. X-ray diffractograms of selected lithologies from Site 1227. **A.** Black nodule consisting of fluorapatite (11.02 mbsf). **B.** Black silty sediment from lithologic Unit III (47.5 mbsf). **C.** Pinkish carbonate-rich layer in Unit III. **D.** Authigenic dolomite nodule from lithologic Unit IV. **E.** Barite nodule. G = Glauconite, Qz = quartz, Fs = feldspar, Ap = apatite, P = pyrite, Cc = calcite, Do = dolomite, Ba = barite.

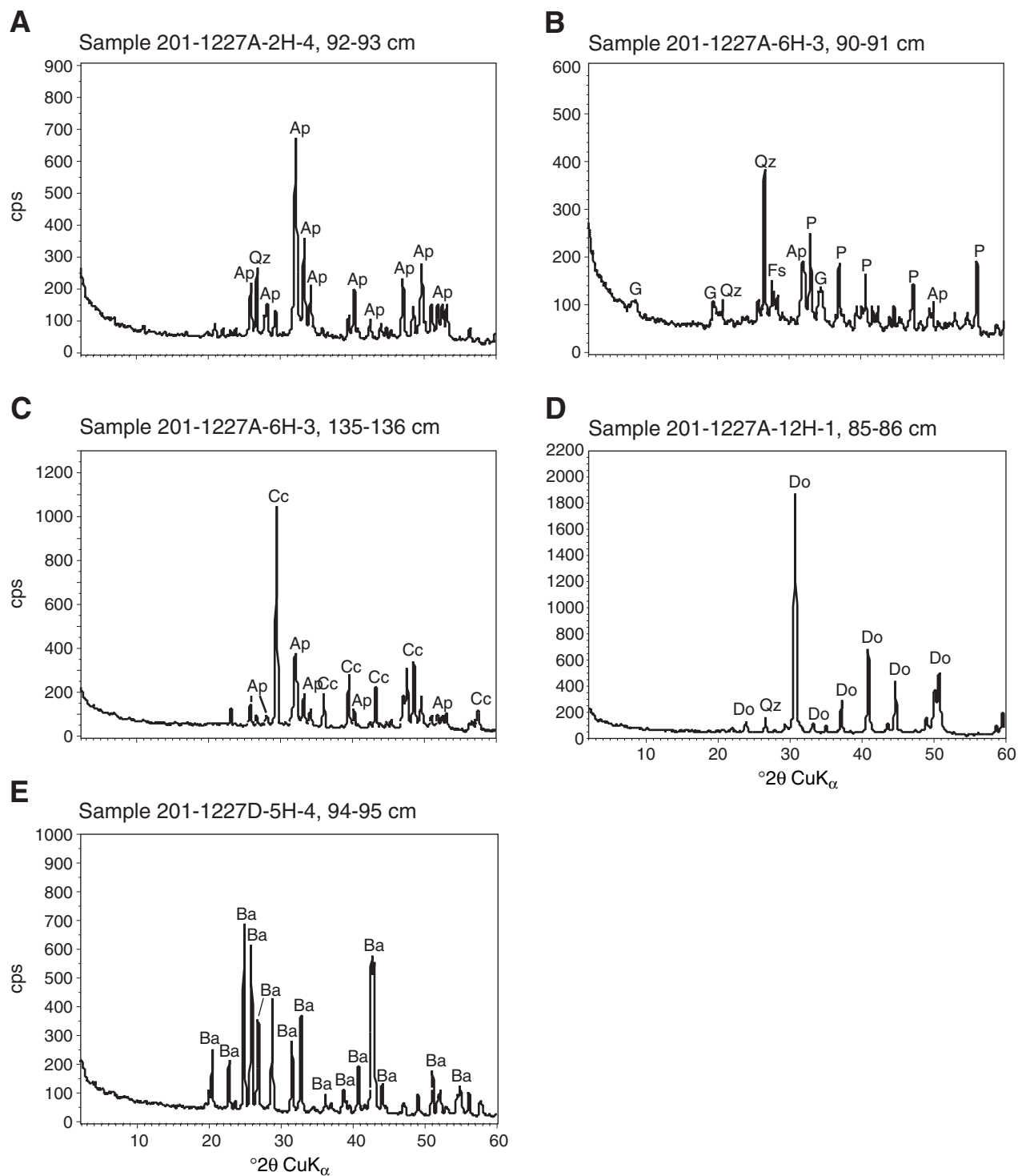


Figure F6. Concentrations of various dissolved species in interstitial waters from Holes 1227A and 1227D. Methane and ethane concentrations in interstitial waters were calculated from 24-hr extraction yields and the porosity estimates derived from gamma ray attenuation densitometer data (see “**Density and Porosity**,” p. 23, in “Physical Properties”). A. Alkalinity. B. Dissolved organic carbon (DIC). C. Sulfate. D. Barium. E. Manganese. F. Iron. G. Strontium. (Continued on next three pages.)

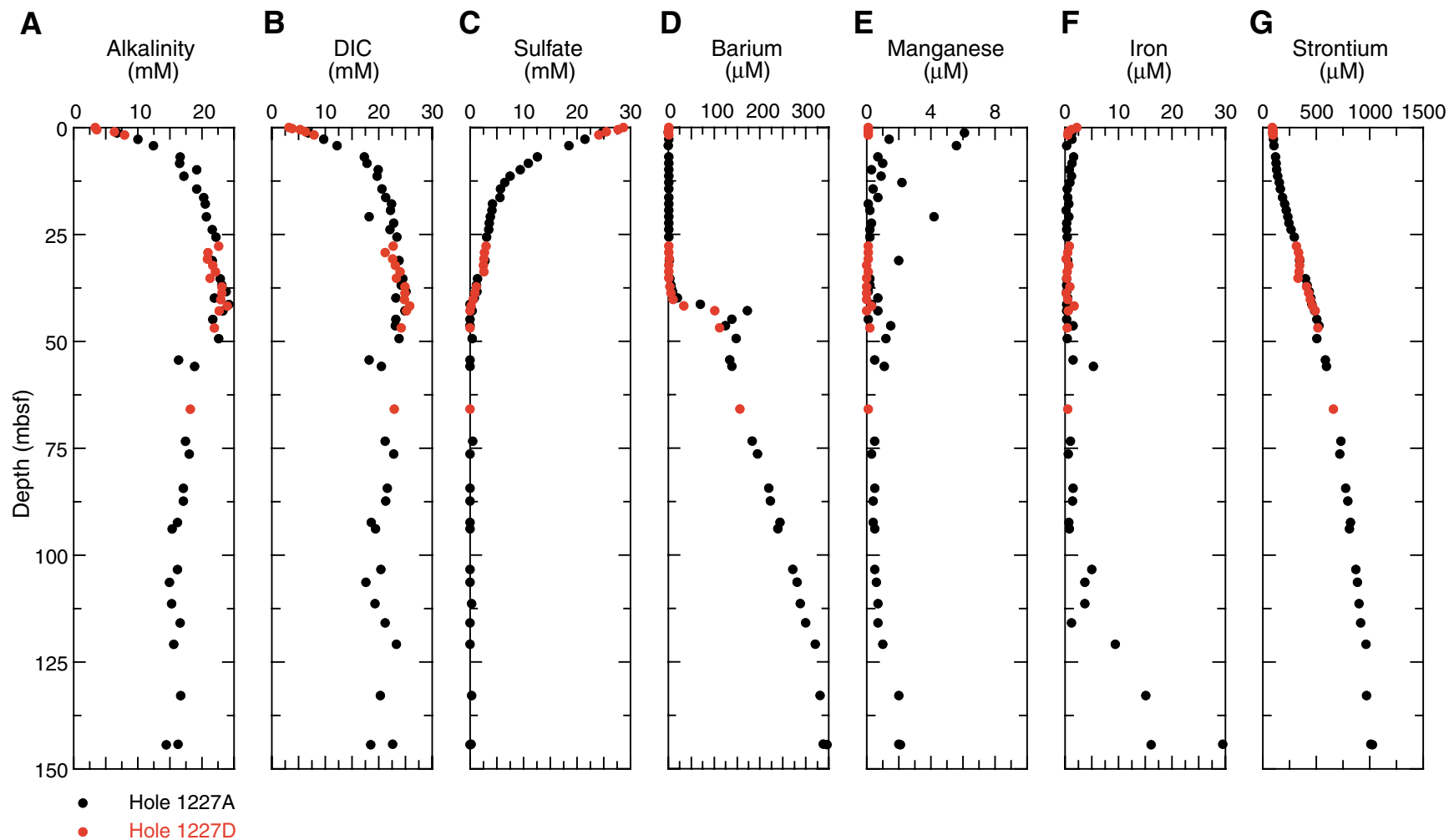


Figure F6 (continued). H. Lithium. I. Total sulfide. J. Acetate. K. Formate. L. Methane. M. Ethane. N. Methane/ethane ratio. (Continued on next page.)

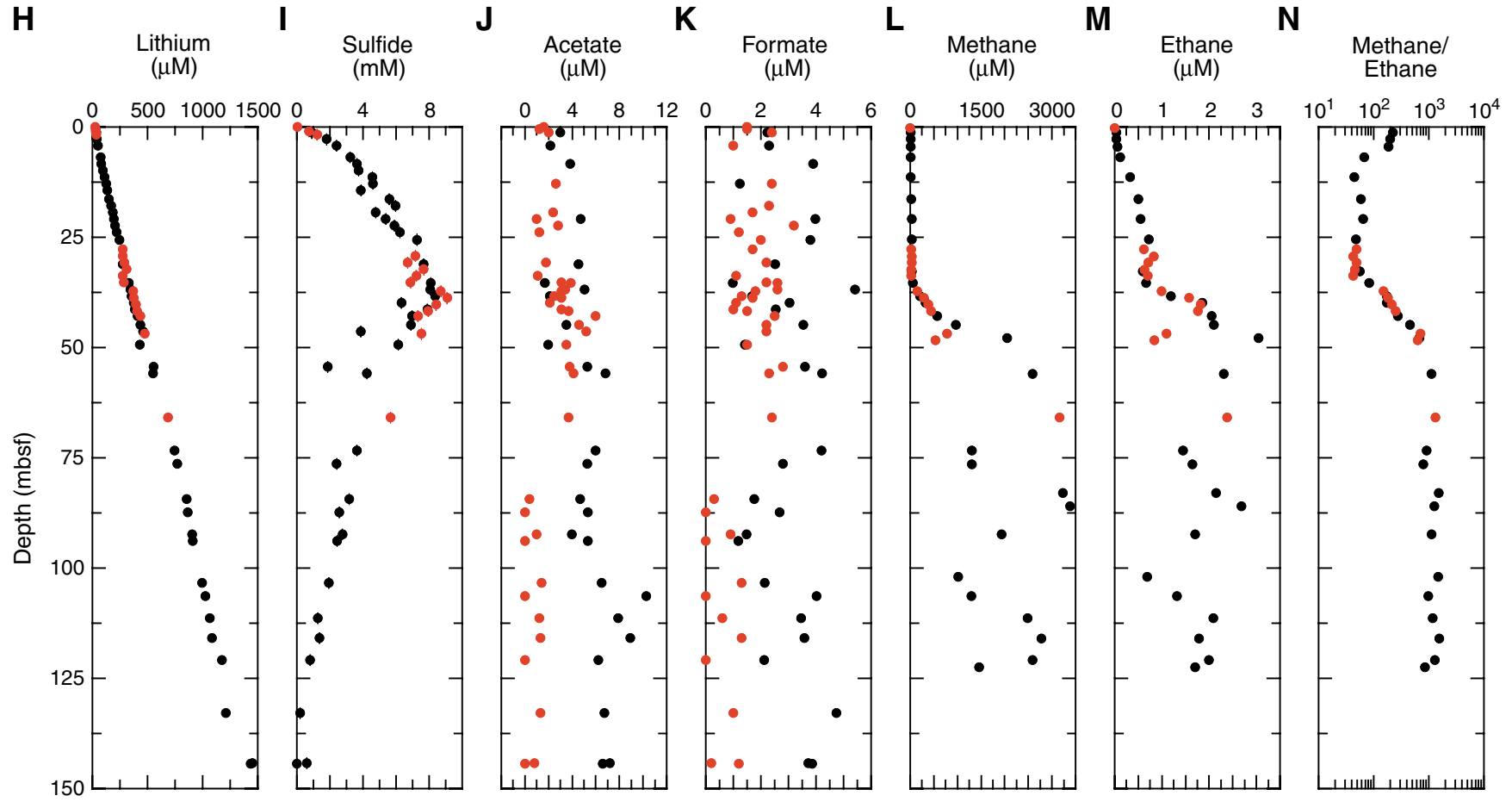


Figure F6 (continued). O. Propane. P. Hydrogen. Q. Ammonium. R. Phosphate. S. Silica. T. chloride. (Continued on next page.)

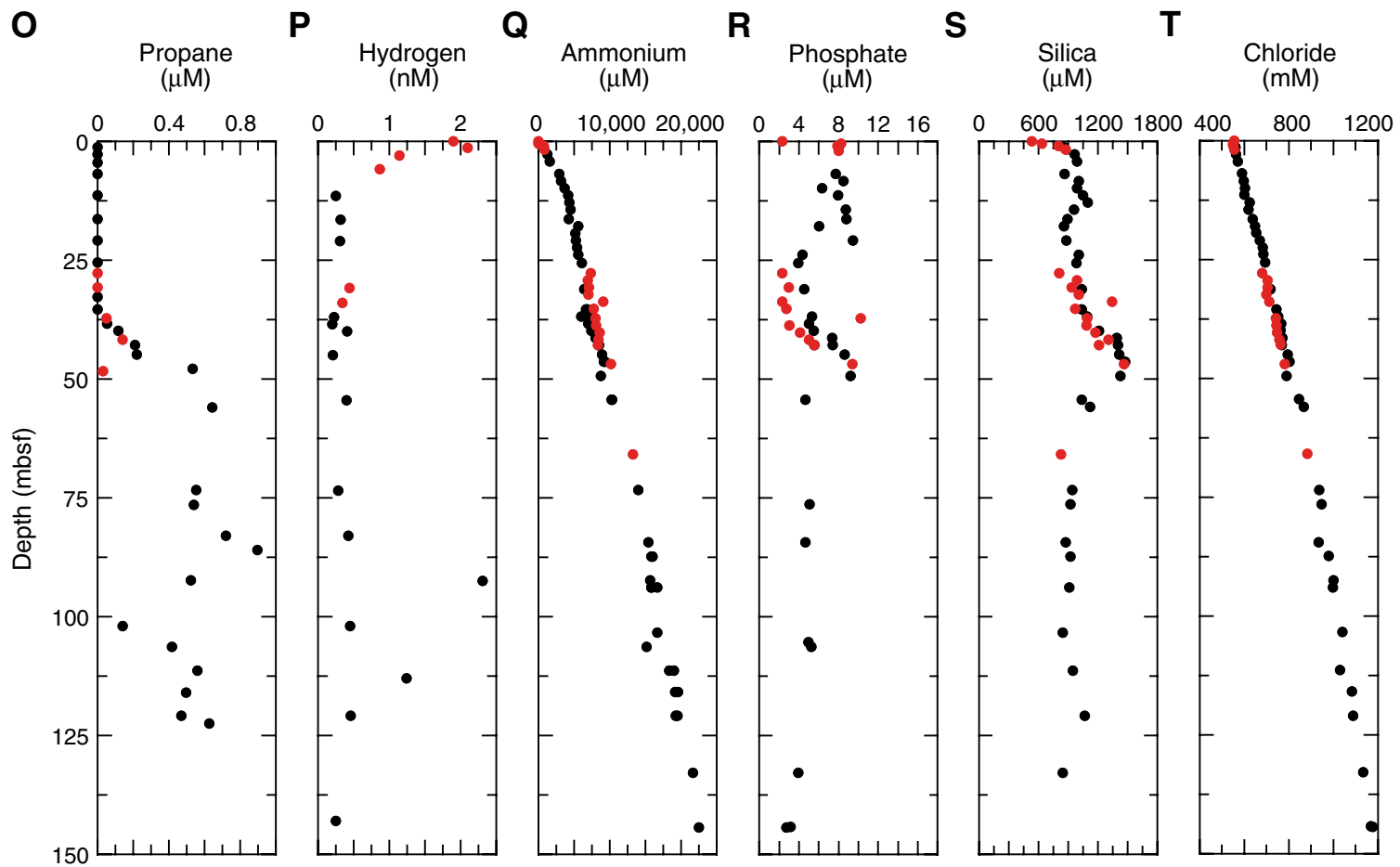


Figure F6 (continued). U. Lithium vs. chloride.

U

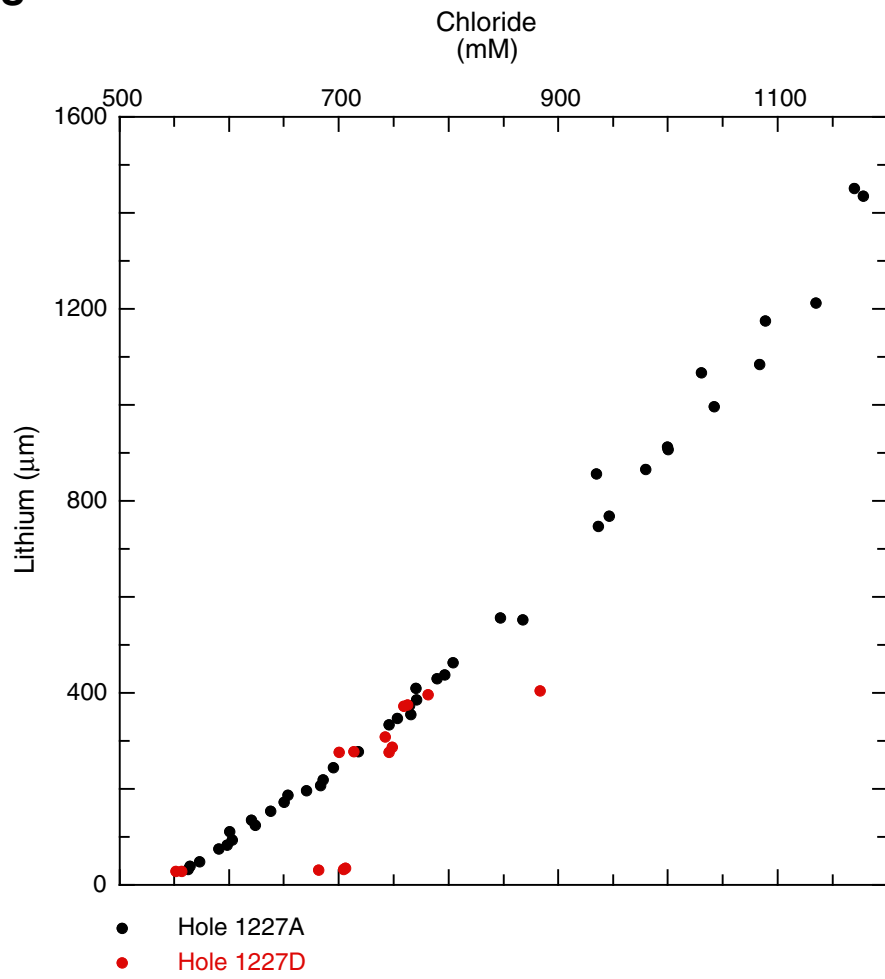


Figure F7. Plot showing correlation between Site 1227 dissolved phosphate and magnetic susceptibility profiles.

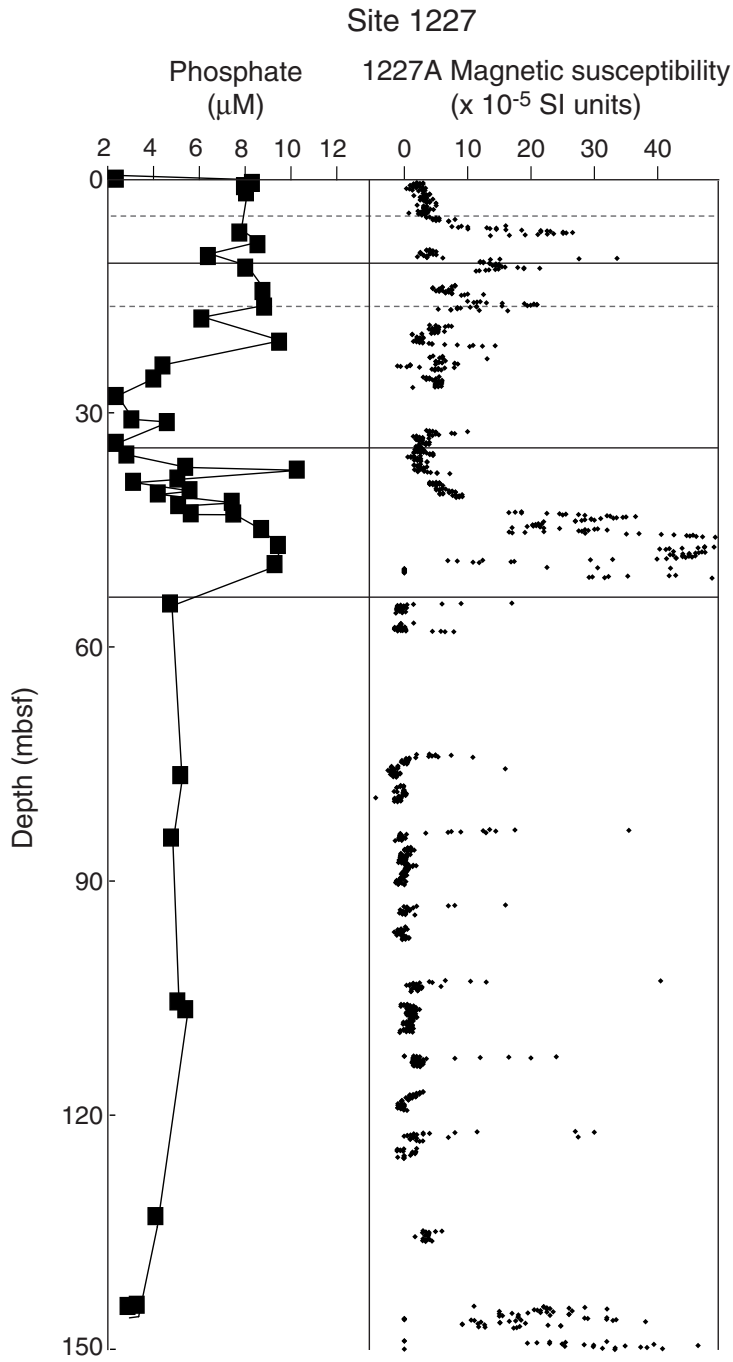


Figure F10. Total prokaryotic cells (solid circles) and the percentage of cell numbers involved in cell division (open circles) with depth at Site 1227. Dividing cell percentages become increasingly unreliable as total cell counts decrease below 2×10^6 cells/cm³ as within-sample variability rises due to the low number of cells counted. Vertical dashed line on the left represents the detection limit at 1.3×10^5 cells/cm³.

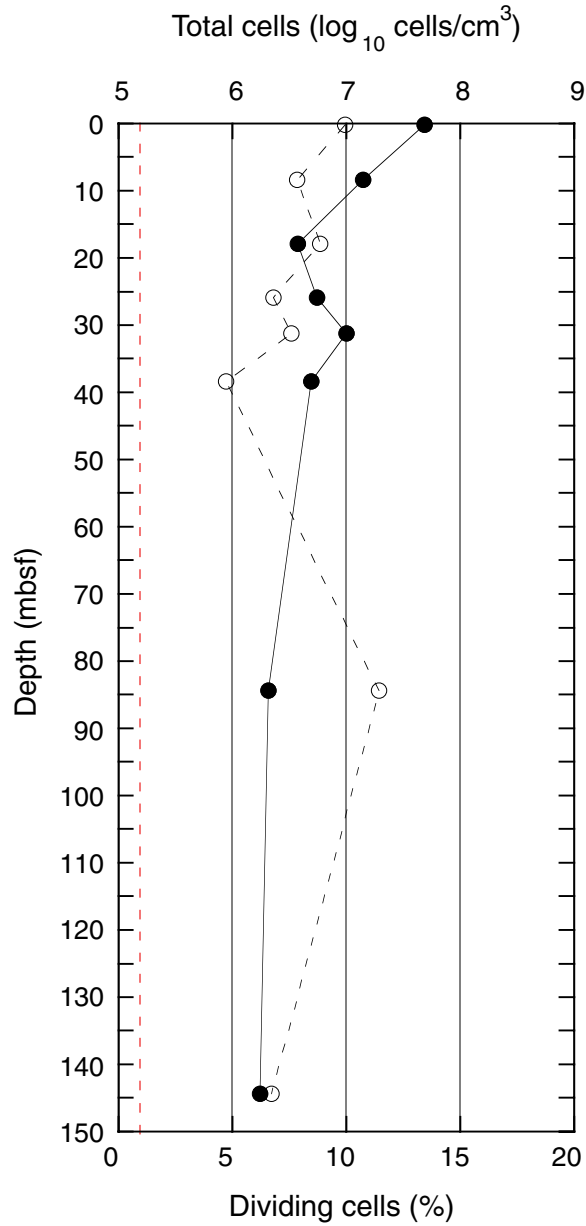


Figure F11. Profile of total prokaryotic cells at Holes 1227D (upper datum) and 1227A (rest of data). Heavy dashed line is a regression line derived from previous ODP legs and updated from Parkes et al. (1994) (\log_{10} cells = $8.03 - 0.66 \log_{10}$ depth); lighter dashed lines are the $\pm 2\text{-}\sigma$ envelopes of cell concentrations from previously censused ODP sites.

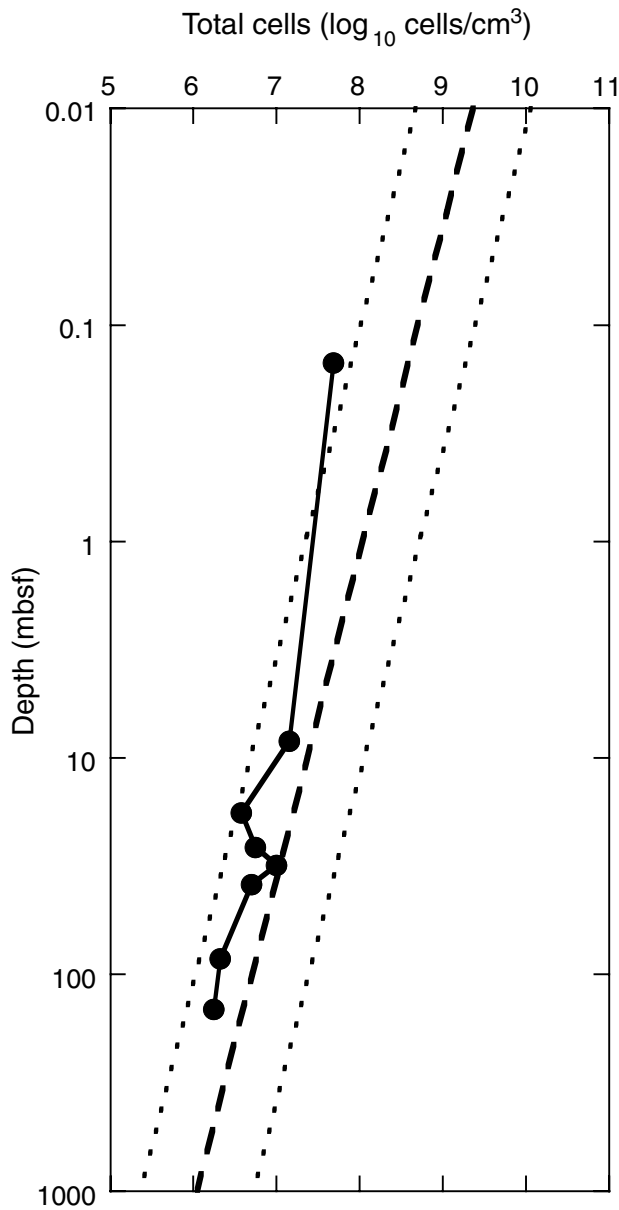


Figure F12. A. Comparison of magnetic susceptibility data from Leg 112 postcruise study of Site 684 (Merrill et al., 1990) with the multisensor track data from Holes 1227A and 1227D. B. Section from 0 to 60 mbsf showing the details and correlation of the individual susceptibility bands between Holes 1227A and 1227D.

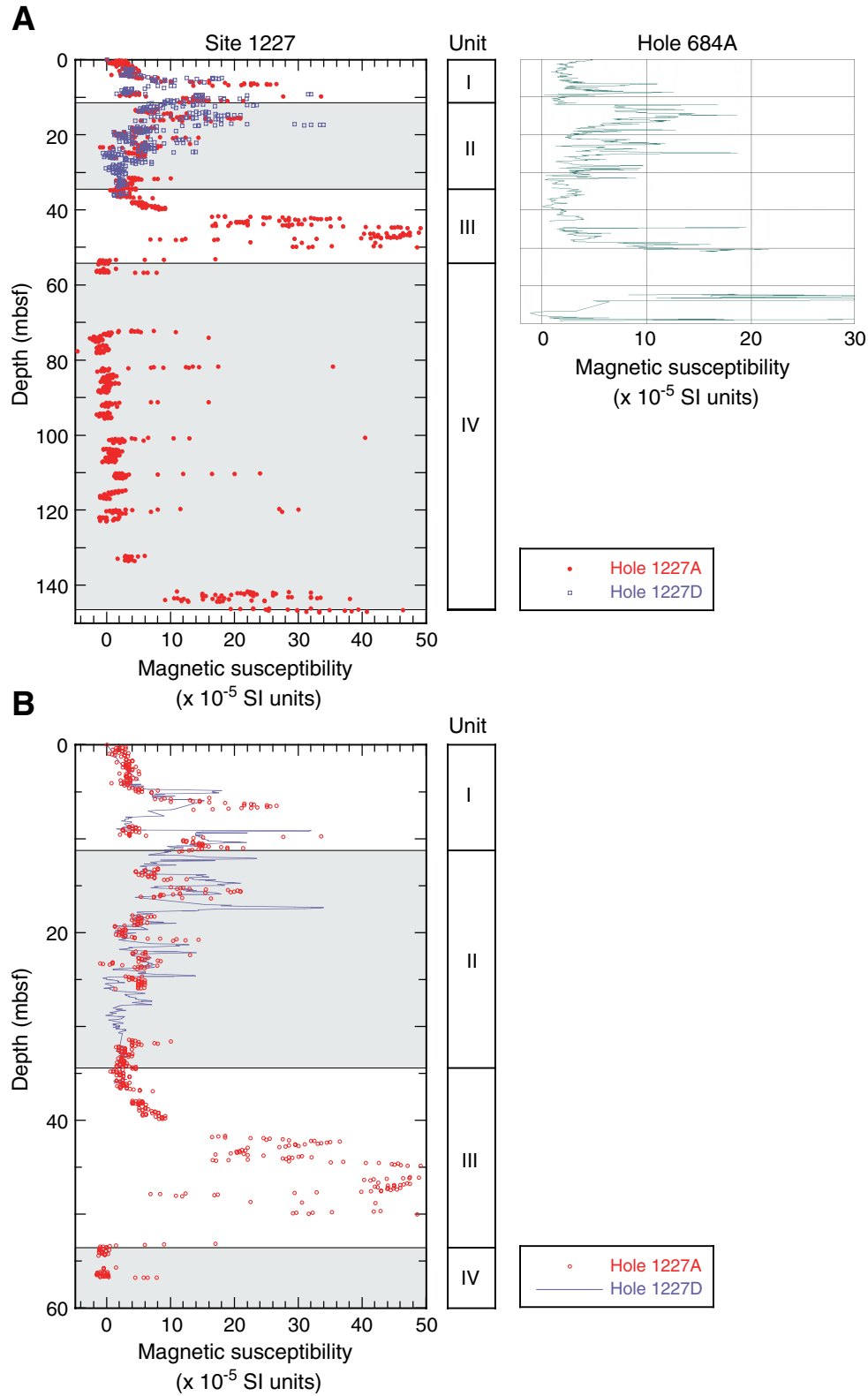


Figure F13. Magnetic intensity and susceptibility in Hole 1227A. Open squares = NRM intensity, solid squares = intensity after 20-mT AF demagnetization.

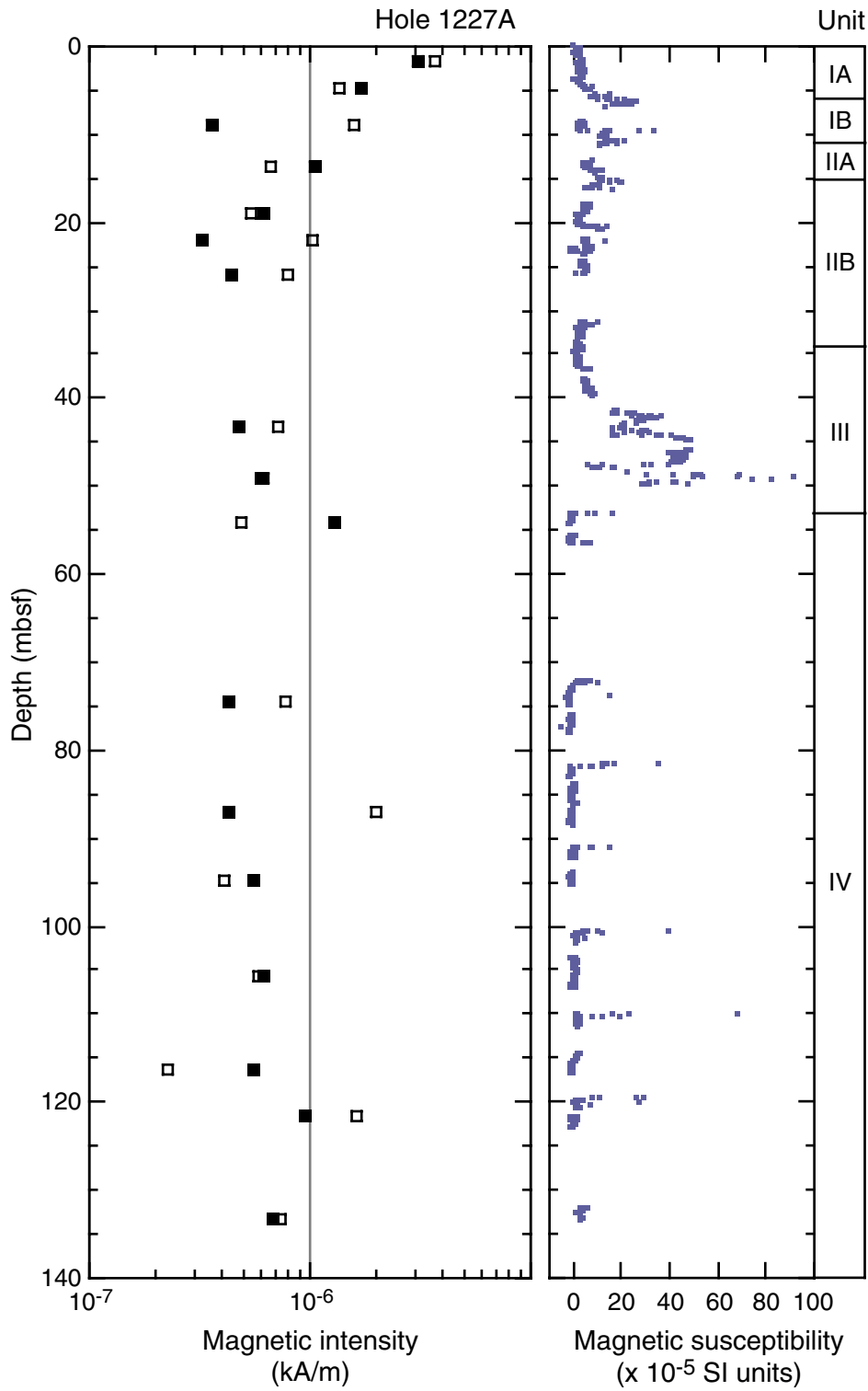


Figure F14. Principal component analysis of natural remanent magnetization (NRM) of Sample 201-1227A-1H-2, 14–16 cm, including equal area projection of directions of magnetization during demagnetization, intensity of magnetization plotted vs. demagnetization, and vector component diagrams showing projection of magnetic vector's endpoints on horizontal and vertical planes.

Sample 201-1227A-1H-2, 14-16 cm

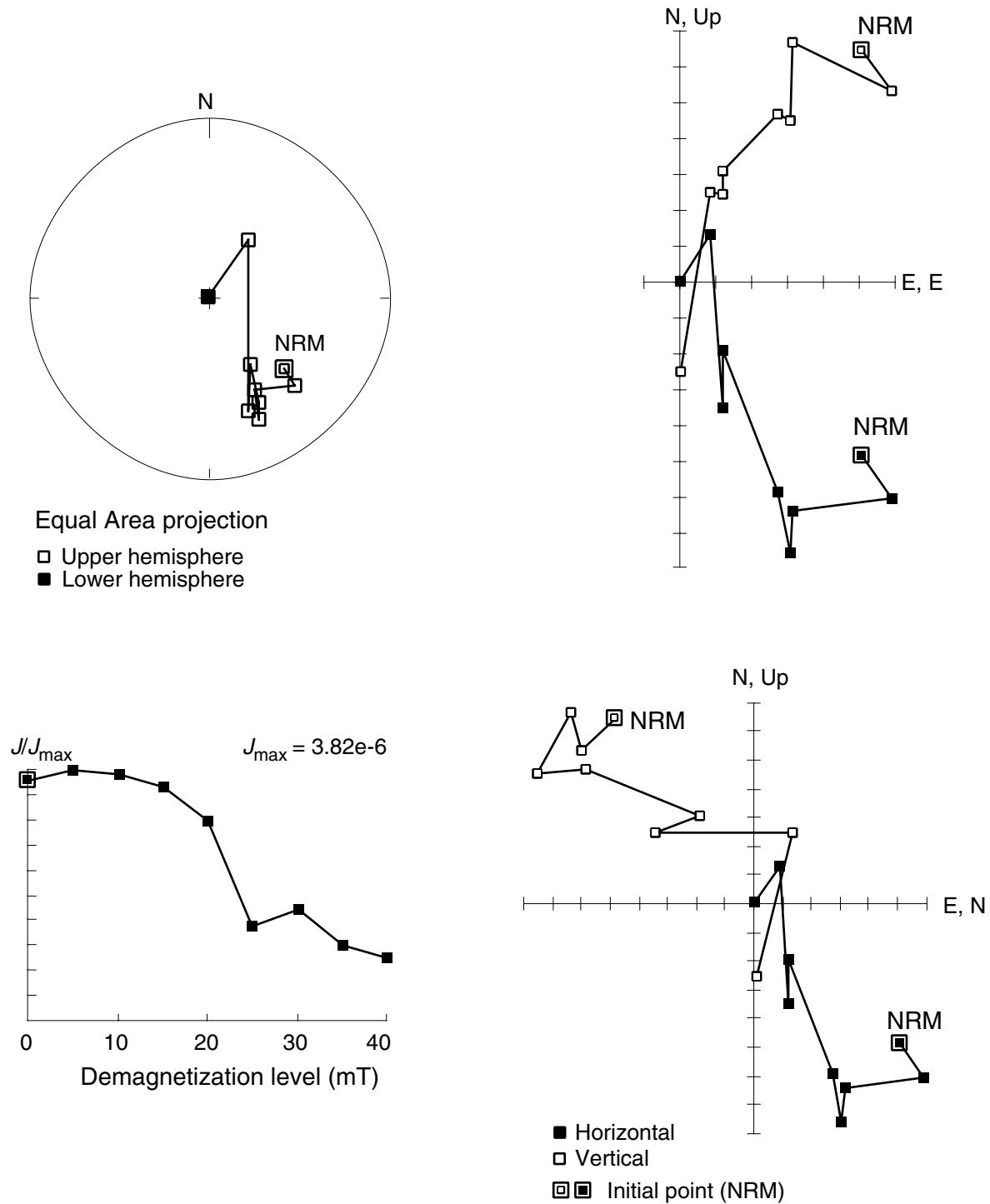


Figure F15. A. Comparison of gamma ray attenuation (GRA) bulk density data from Holes 1227A and 1227D with those from Hole 684C. B. Section from 0 to 60 mbsf showing the details and correlation of bulk density bands between Holes 1227A and 1227D.

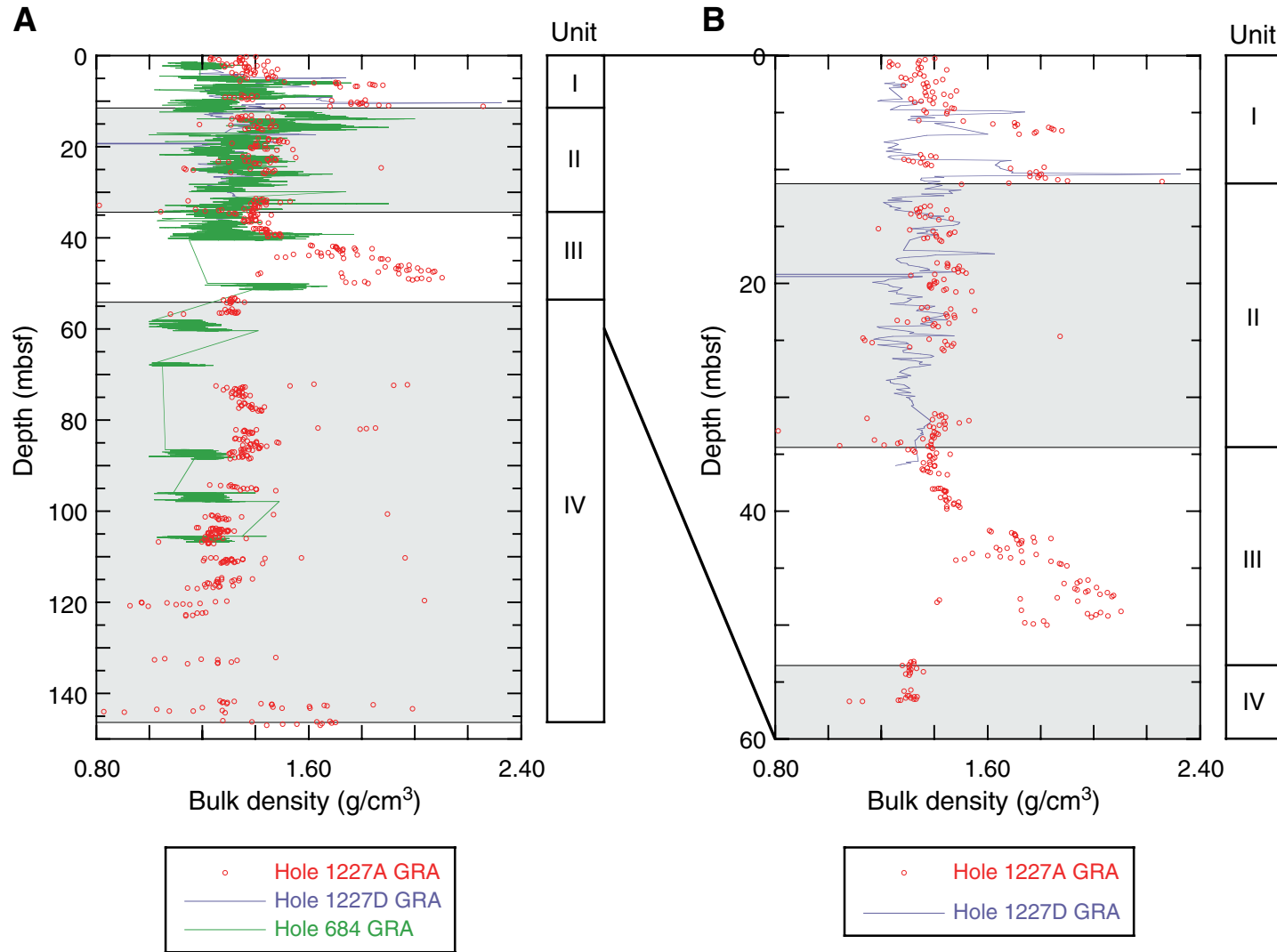


Figure F16. Comparison of 5-m moving averages of gamma ray attenuation (GRA) bulk density from Holes 1227A, 684A, and mass/volume moisture and density (MAD)-based densities measured on samples from Hole 1227A. The data are in reasonable agreement in lithostratigraphic Units I and II, but diverge markedly in the zones of low recovery.

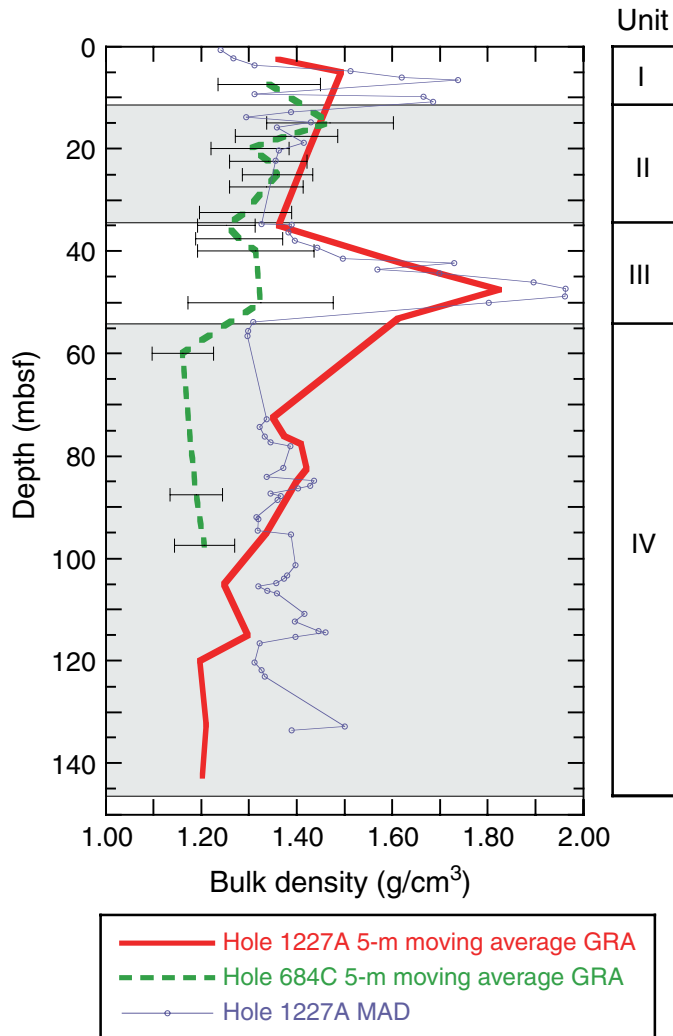


Figure F17. Mass/volume moisture and density (MAD) measurements for Hole 1227A. **A.** Gamma ray attenuation (GRA) and moisture and density (MAD) bulk density profiles. **B.** Hole 1227A grain density profile. **C.** Porosity profile. Note porosity lows associated with the coarse-grained strata of Units I and III.

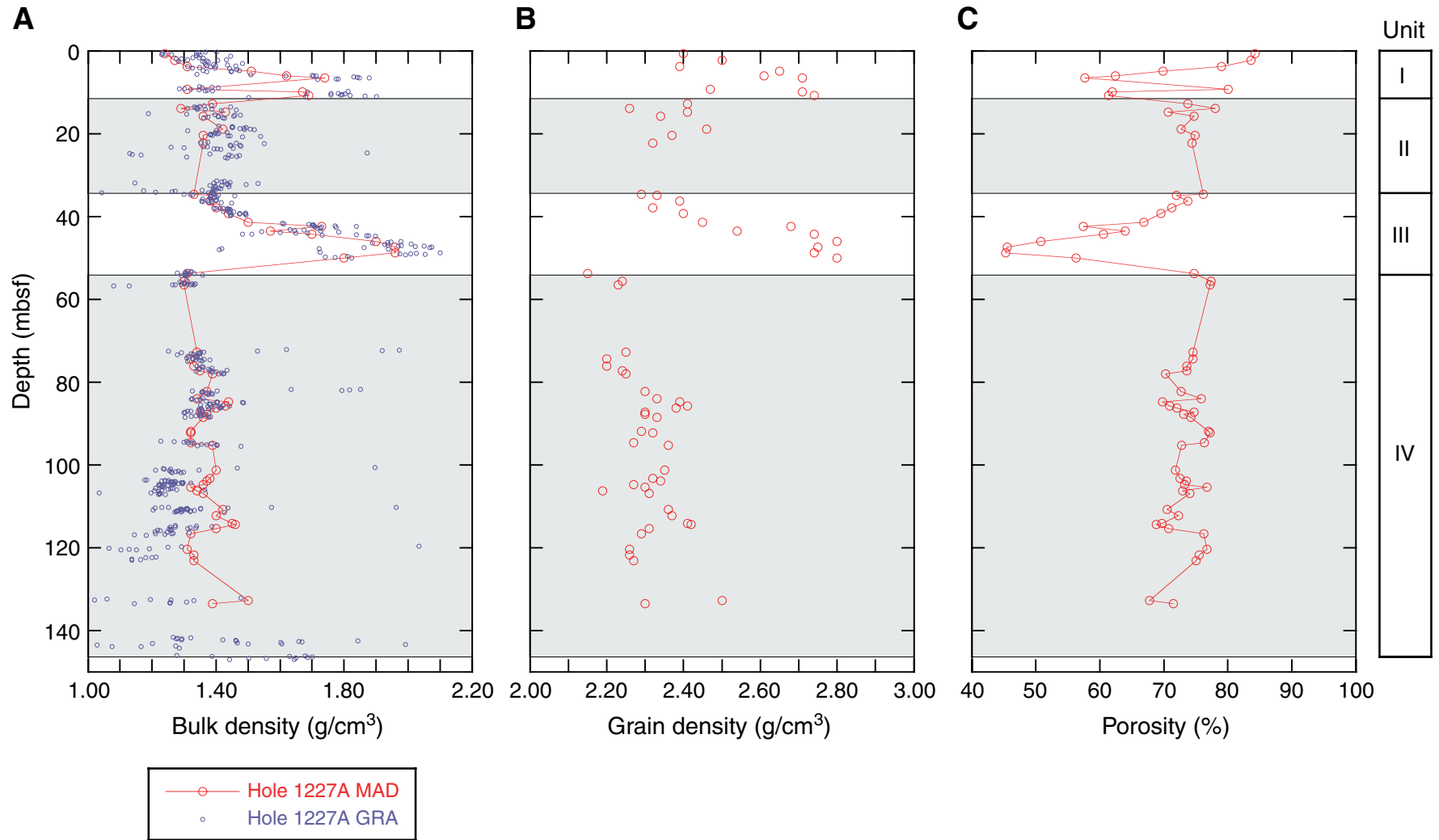


Figure F18. *P*-wave velocity profiles derived from *P*-wave logger (PWL) and PWS3 measurements for Site 1227. Thick dark blue lines provide an interpretation of the PWS3 measurements consistent with litho-stratigraphic changes. The thin aqua-blue line projects PWS3 velocities from the changes in PWL measurements. Relative to the ooze sediments making up the dominant lithology of the upper 55 mbsf, the two coarse-grained silts beginning at ~6.2 and 42.0 mbsf are clearly defined by a 150-m/s increase in *P*-wave velocity.

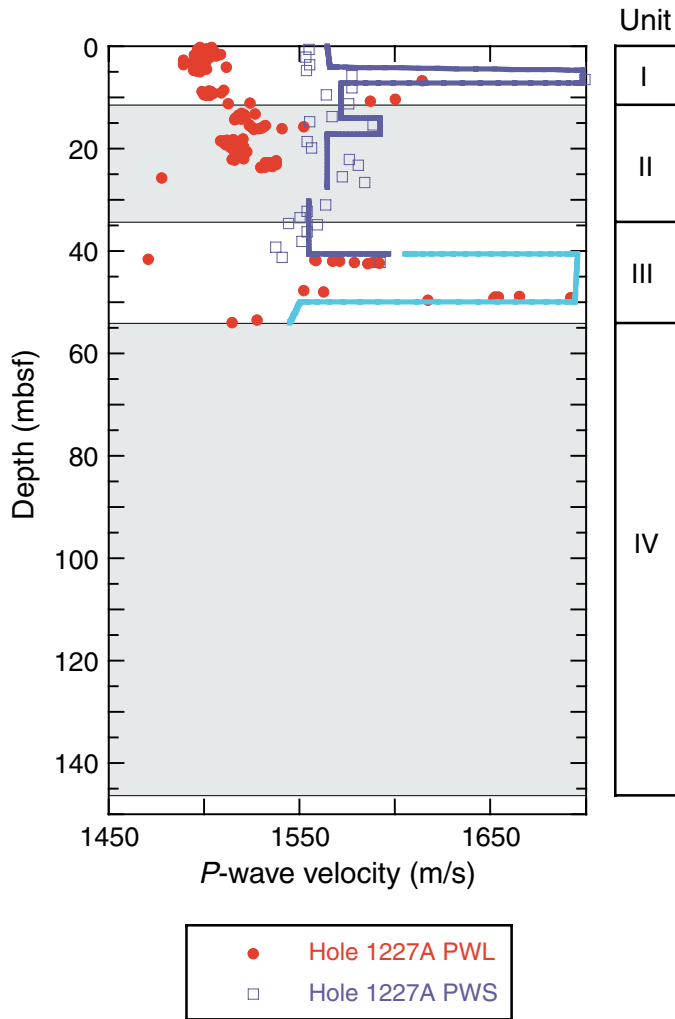


Figure F19. Natural gamma radiation (NGR) profile for Hole 1227A. Gamma ray emission peaks in Units I and III probably arise from the decay of radioactive potassium in glauconite, a common constituent of these layers.

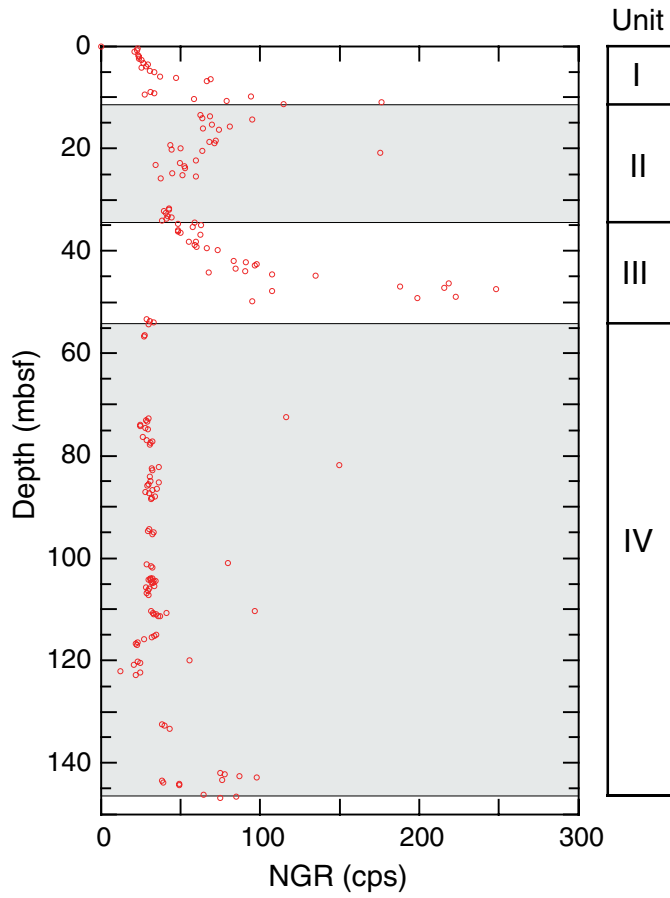


Figure F20. Thermal conductivity measurements for Hole 1227A. A. Thermal conductivity profile (needle probe method). B. Mean-detrended bulk density and thermal conductivity profiles illustrate the controlling effect of water content variability on thermal properties.

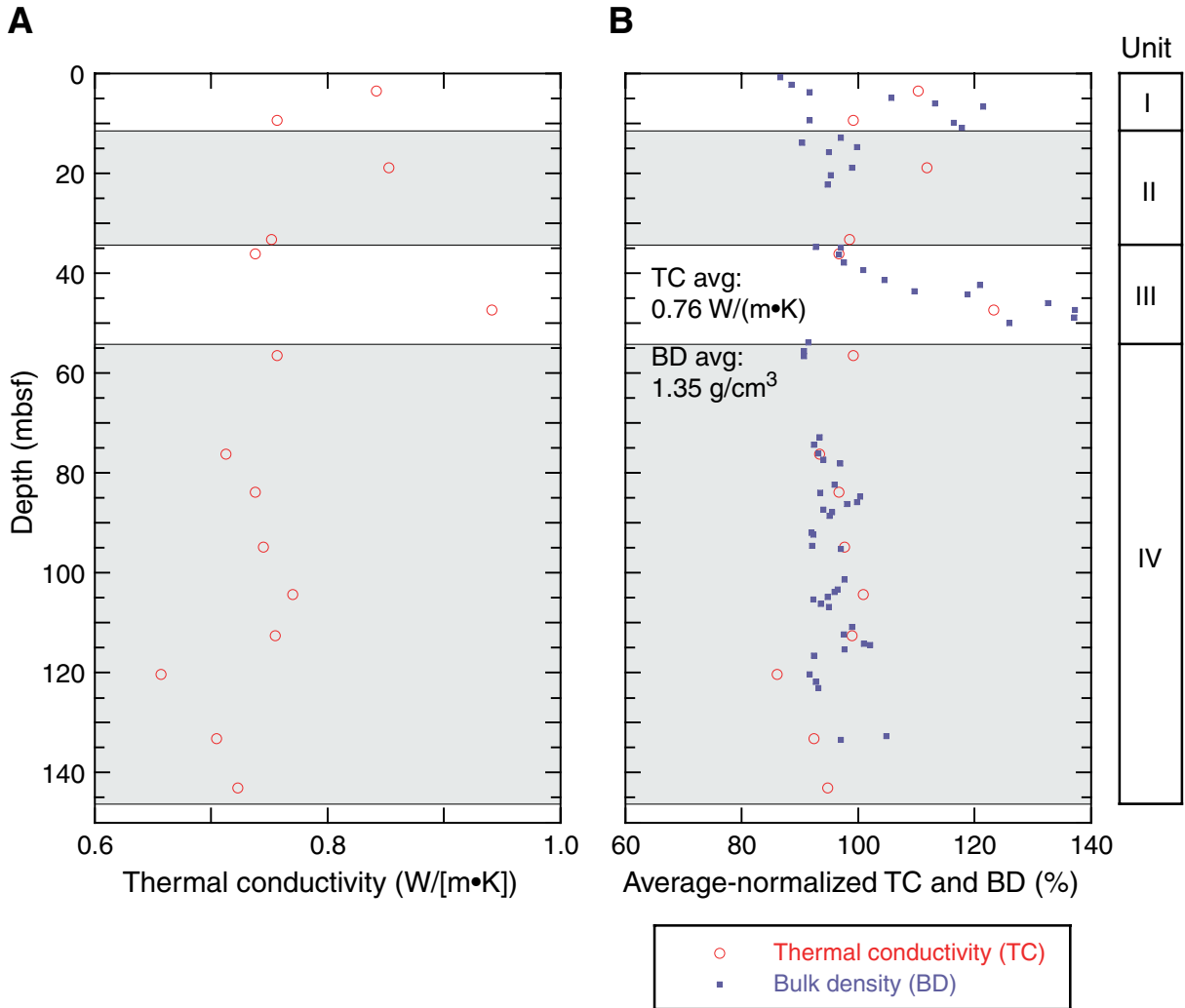


Figure F21. Formation factor profile for Site 1227A. The coarse-grained lenses beginning at ~6.2 and 42.0 mbsf, respectively, are clearly defined. No significant consolidation trend resulting from diagenetic or framework compaction is evident in this profile.

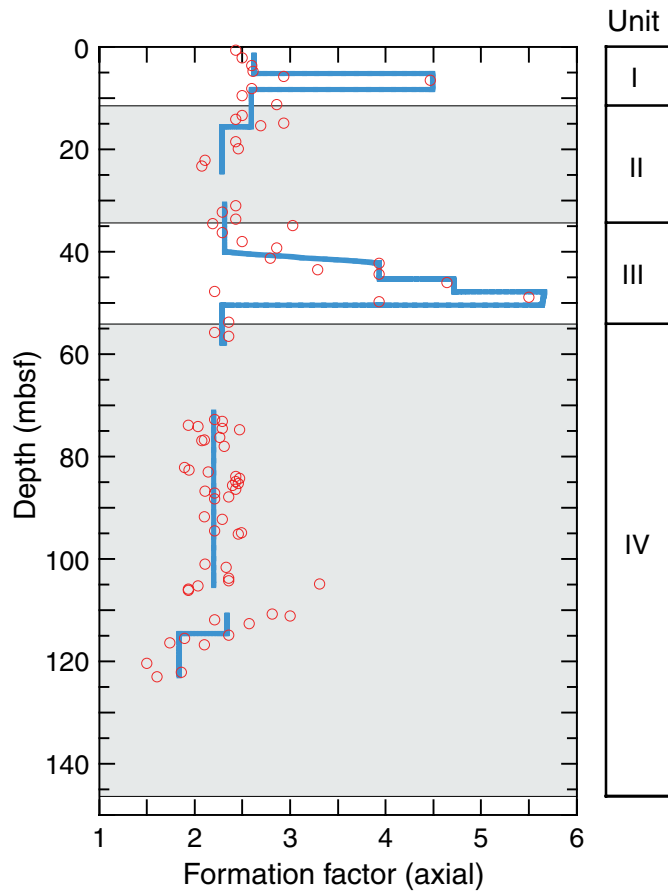


Figure F22. Temperature records from the two DVTP deployments at Site 1227 together with the extrapolated temperature. A. Record for the lower thermistor from the deployment after Core 201-1227A-9H at 81.6 mbsf. B. Records for both thermistors from the deployment after Core 201-1227A-12H at 110.1 mbsf. The data from the upper thermistor were used for the temperature extrapolation.

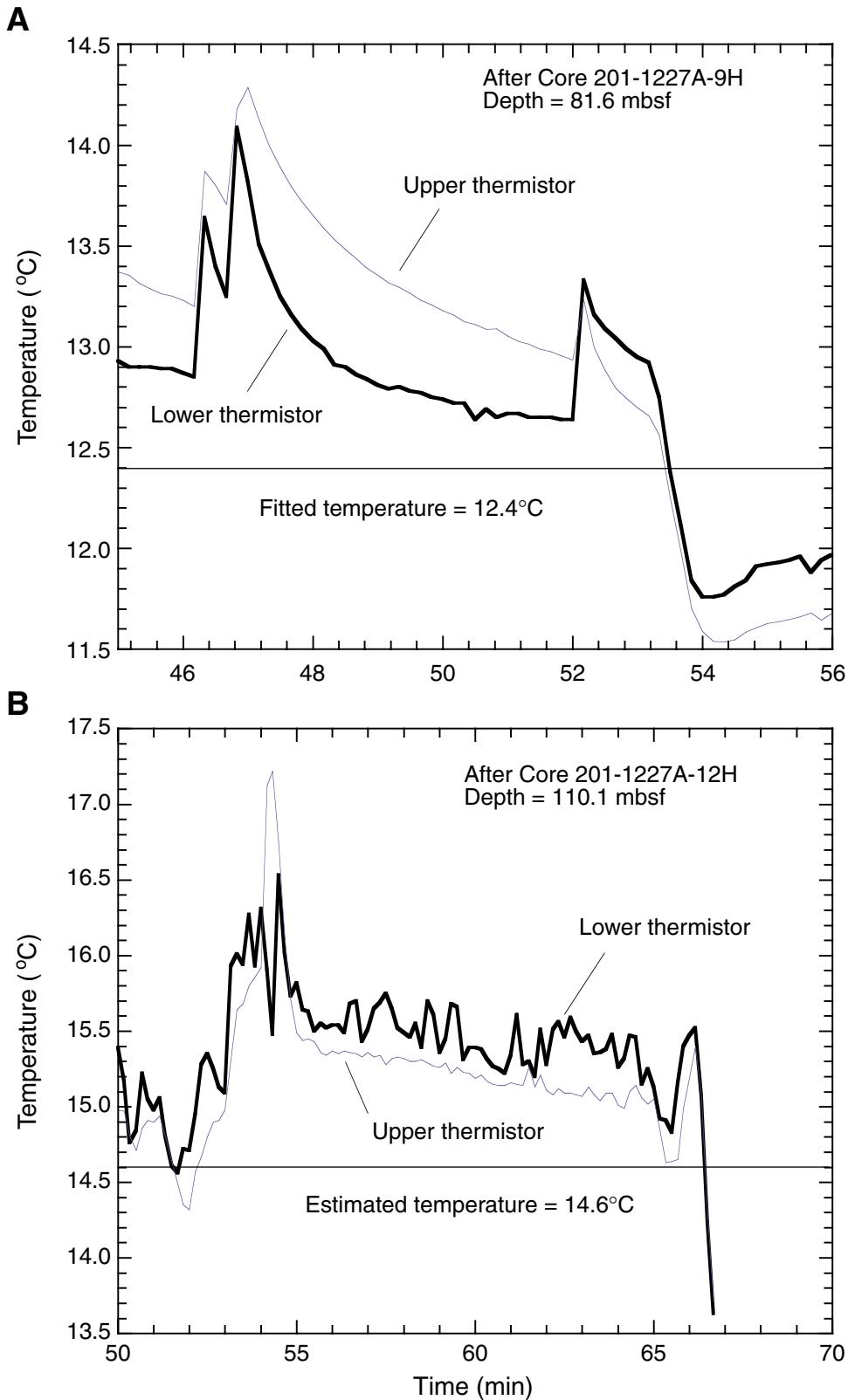


Figure F23. All temperatures measured in Hole 1227A together with the temperature data from Site 684 plotted vs. depth with a best-fit linear profile for the combined data.

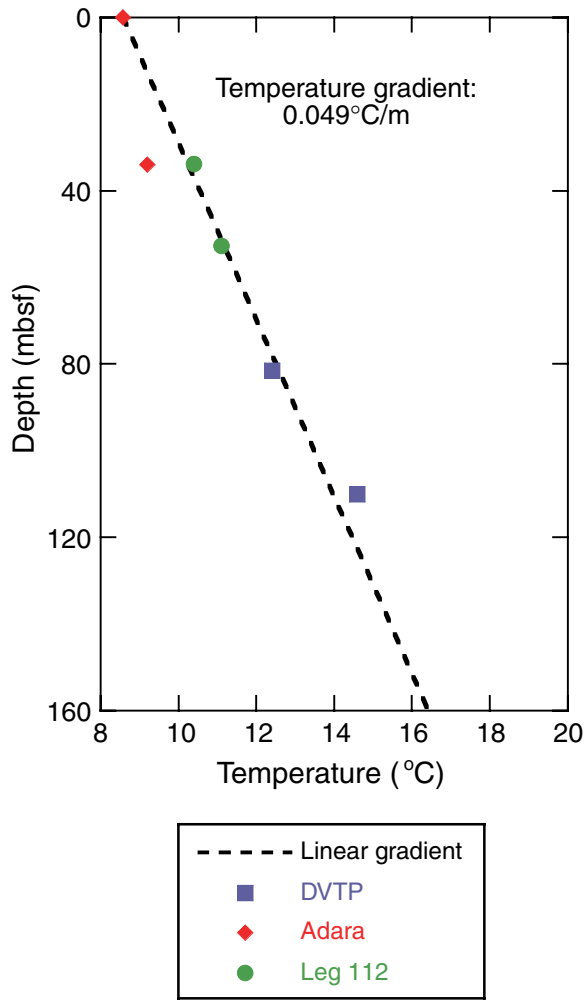


Figure F24. Pressure measured in Hole 1227A during the DVTP-P station after Core 201-1227-14H. Rapid drop-off at the start of the 30-min equilibration period indicates that the formation did not form an adequate seal around the probe.

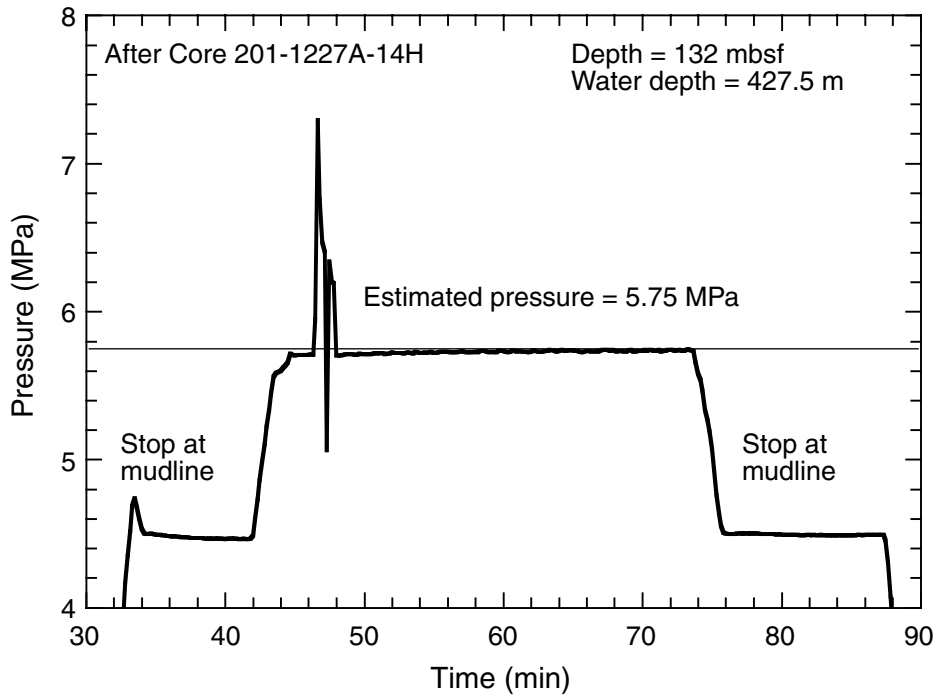


Table T1. Coring summary, Site 1227. (Continued on next page.)

Hole 1227A

Latitude: 8°59.4631'S
Longitude: 79°57.3499'W
Time on site (hr): 61.75 (1300 hr, 28 Feb–0245 hr, 3 Mar 2002)
Time on hole (hr): 40.83 (1300 hr, 28 Feb–0550 hr, 2 Mar 2002)
Seafloor (drill pipe measurement from rig floor, mbrf): 438.9
Distance between rig floor and sea level (m): 11.4
Water depth (drill pipe measurement from sea level, m): 427.5
Total depth (drill pipe measurement from rig floor, mbrf): 590.0
Total penetration (meters below seafloor, mbsf): 151.1
Total length of cored section (m): 151.1
Total core recovered (m): 100.51
Core recovery (%): 66.5
Total number of cores: 18

Hole 1227B

Latitude: 8°59.4528'S
Longitude: 79°57.3503'W
Time on hole (hr): 2.67 (0550 hr, 2 Mar–0830 hr, 2 Mar 2002)
Seafloor (drill pipe measurement from rig floor, mbrf): 438.5
Distance between rig floor and sea level (m): 11.4
Water depth (drill pipe measurement from sea level, m): 427.1
Total depth (drill pipe measurement from rig floor, mbrf): 462.5
Total penetration (meters below seafloor, mbsf): 24.0
Total length of cored section (m): 24.0
Total core recovered (m): 24.67
Core recovery (%): 102.8
Total number of cores: 3

Hole 1227C

Latitude: 8°59.4468'S
Longitude: 79°57.3475'W
Time on hole (hr): 1.33 (0830 hr, 2 Mar–0950 hr, 2 Mar 2002)
Seafloor (drill pipe measurement from rig floor, mbrf): 437.7
Distance between rig floor and sea level (m): 11.4
Water depth (drill pipe measurement from sea level, m): 426.3
Total depth (drill pipe measurement from rig floor, mbrf): 464.5
Total penetration (meters below seafloor, mbsf): 26.8
Total length of cored section (m): 26.8
Total core recovered (m): 27.25
Core recovery (%): 101.7
Total number of cores: 3

Hole 1227D

Latitude: 8°59.4474'S
Longitude: 79°57.3613'W
Time on hole (hr): 11.92 (0950 hr, 2 Mar–2145 hr, 2 Mar 2002)
Seafloor (drill pipe measurement from rig floor, mbrf): 438.0
Distance between rig floor and sea level (m): 11.4
Water depth (drill pipe measurement from sea level, m): 426.6
Total depth (drill pipe measurement from rig floor, mbrf): 512.0
Total penetration (meters below seafloor, mbsf): 74.0
Total length of cored section (m): 74.0
Total core recovered (m): 54.84
Core recovery (%): 74.1
Total number of cores: 8

Hole 1227E

Latitude: 8° 59.4416'S
Longitude: 79°57.3598'W
Time on hole (hr): 5 (2145 hr, 2 Mar–0245 hr, 3 Mar 2002)
Seafloor (drill pipe measurement from rig floor, mbrf): 438.6
Distance between rig floor and sea level (m): 11.4
Water depth (drill pipe measurement from sea level, m): 427.2
Total depth (drill pipe measurement from rig floor, mbrf): 465.5
Total penetration (meters below seafloor, mbsf): 26.0
Total length of cored section (m): 26.9
Total core recovered (m): 26.72
Core recovery (%): 99.33
Total number of cores: 4

Table T1 (continued).

Core	Date (2002)	Local time (hr)	Depth (mbsf)		Length (m)		Recovery (%)
			Top	Bottom	Cored	Recovered	
201-1227A-							
1H	28 Feb	1805	0.0	5.6	5.6	5.59	99.8
2H	28 Feb	1915	5.6	15.1	9.5	9.81	103.3
3H	28 Feb	2130	15.1	24.6	9.5	9.86	103.8
4H	1 Mar	0055	24.6	34.1	9.5	10.97	115.5
5H	1 Mar	0245	34.1	43.6	9.5	9.74	102.5
6H	1 Mar	0415	43.6	53.1	9.5	6.47	68.1
7H	1 Mar	0625	53.1	62.6	9.5	3.72	39.2
8H	1 Mar	0825	62.6	72.1	9.5	0.38	4.0
9H	1 Mar	1035	72.1	81.6	9.5	6.48	68.2
10H	1 Mar	1300	81.6	91.1	9.5	7.36	77.5
11H	1 Mar	1500	91.1	100.6	9.5	4.45	46.8
12H	1 Mar	1700	100.6	110.1	9.5	7.00	73.7
13H	1 Mar	1930	110.1	119.6	9.5	7.26	76.4
14H	1 Mar	2030	119.6	129.1	9.5	3.82	40.2
15P	1 Mar	2140	129.1	131.1	2.0	0.00	0.0
16M	1 Mar	2245	131.1	132.1	1.0	0.15	15.0
17H	2 Mar	0050	132.1	141.6	9.5	1.63	17.2
18H	2 Mar	0415	141.6	151.1	9.5	5.82	61.3
Cored totals:					151.1	100.51	66.5
201-1227B-							
1H	2 Mar	0705	0.0	5.0	5.0	5.04	100.8
2H	2 Mar	0725	5.0	14.5	9.5	9.98	105.1
3H	2 Mar	0755	14.5	24.0	9.5	9.65	101.6
Cored totals:					24.0	24.67	102.8
201-1227C-							
1H	2 Mar	0850	0.0	7.8	7.8	7.77	99.6
2H	2 Mar	0905	7.8	17.3	9.5	9.48	99.8
3H	2 Mar	0935	17.3	26.8	9.5	10.00	105.3
Cored totals:					26.8	27.25	101.7
201-1227D-							
1H	2 Mar	1115	0.0	7.5	7.5	7.53	100.4
2H	2 Mar	1140	7.5	17.0	9.5	9.14	96.2
3H	2 Mar	1215	17.0	26.5	9.5	9.97	105.0
4H	2 Mar	1250	26.5	36.0	9.5	9.87	103.9
5H	2 Mar	1625	36.0	45.5	9.5	7.38	77.7
6H	2 Mar	1825	45.5	55.0	9.5	9.15	96.3
7H	2 Mar	1935	55.0	64.5	9.5	0.10	1.1
8H	2 Mar	2030	64.5	74.0	9.5	1.70	17.9
Cored totals:					74.0	54.84	74.1
201-1227E-							
1H	2 Mar	2215	0.0	6.9	6.9	6.90	100.0
2H	2 Mar	2235	6.9	16.4	9.5	9.63	101.4
3H	2 Mar	2300	16.4	25.9	9.5	9.75	102.6
4M	2 Mar	2350	25.9	26.9	1.0	0.44	44.0
Cored totals:					26.9	26.72	99.3

Table T2. Concentrations of dissolved species in interstitial waters, Holes 1227A and 1227D. (See table notes. Continued on next page.)

Core, section, interval (cm)	Depth (mbsf)	pH	Alk (mM)	DIC (mM)	Cl ⁻ (mM)	SO ₄ ²⁻ (mM)	H ₄ SiO ₄ (μM)	PO ₄ ³⁻ (μM)	NH ₄ ⁺ (μM)	Fe (μM)	Mn (μM)	Sr (μM)	Li (μM)	Ba (μM)	ΣH ₂ S (mM)	Acetate (μM)	Formate (μM)
201-1227A-																	
1H-1, 135-150	1.35	7.65	6.74	6.76	563	24.7	856		680	1.3	6.1	96	32.3	0.4	0.92	1.6	1.5
1H-2, 135-150	2.85	7.31	9.98	9.67	565	21.5	965		1,200	1.3	1.4	100	39.0	0.5	1.80		
1H-3, 135-150	4.35	7.18	12.46	12.18	574	18.5	993		1,630	0.3	5.6	104	47.9	0.4	2.40	1.2	1.5
2H-1, 135-150	6.95	7.24	16.61	17.34	591	12.6	865	7.74	2,880	1.6	0.7	122	73.9	0.7	3.22		
2H-2, 135-150	8.45	7.29	16.49	17.77	599	10.9	1010	8.53	3,160	1.3	1.0	126	82.9	0.6	3.64	2.0	2.4
2H-3, 135-150	9.95	7.59	19.19	19.88	603	9.4	990	6.36	3,640	0.8	0.3	131	93.9	0.8	3.75		
2H-4, 135-150	11.45	7.76	17.18	19.69	601	7.5	1050	7.99	4,170	1.2	0.9	141	110.6	1.0	4.57		
2H-5, 135-150	12.95				624	6.5	1099		4,330	0.9	2.2	155	123.8	1.0	4.61	*	1.0
2H-6, 135-150	14.45	7.65	19.18	20.63	621	5.7	960	8.74	4,540	0.4	0.4	163	134.3	0.9	3.89		
3H-1, 135-150	16.45	7.43	20.25	21.28	638	5.6	895	8.81	4,290	0.5	0.7	185	152.6	0.8	5.58		
3H-2, 135-150	17.95	7.31	20.49	22.36	650	4.2	858	6.07	5,610	0.7	0.1	204	171.5	1.0	5.97		
3H-3, 135-150	19.45			22.22	654	4.1			5,140	0.2	0.2	218	186.2	1.0	4.76		
3H-4, 135-150	20.95	7.13	20.70	18.23	671	3.8	882	9.47	5,300	0.7	4.2	233	195.1	1.0	5.38	2.6	2.4
3H-5, 135-150	22.45			22.78	684	3.6			5,380	0.3	0.3	245	206.7	1.2	5.90		
3H-6, 135-150	23.95	7.20	21.54	22.13	686	3.5	1010	4.36	5,580	0.3	0.2	265	218.9	1.2	6.23		
4H-1, 102-117	25.62	7.17	22.22	23.38	695	3.1	985	3.96	6,040	0.4	0.2	295	243.1	1.3	7.26	*	2.3
4H-5, 95-110	31.21	6.92	21.62	23.83	718	2.8	1041	4.55	6,380	0.5	2.0	343	277.1	1.9	7.67	2.4	1.7
5H-1, 135-150	35.45	7.00	22.88	24.52	746	1.4	1040		6,720	0.3	0.2	401	333.0	3.6	8.10	1.0	0.9
5H-2, 135-150	36.95	6.99	23.07	24.20	754	1.2	1091	5.35	6,760	0.3	0.2	415	346.7	5.4	8.07	2.8	3.2
5H-3, 135-150	38.45	7.11	23.77	25.05	766	1.3		5.01	7,040	0.3	0.1	434	354.5	8.9	8.36	1.2	1.2
5H-4, 135-150	39.95	7.10	21.95	23.18	764	0.8	1210	5.54	7,440	0.5	0.7	452	373.3	19.8	6.31	*	2.0
5H-5, 135-150	41.45	7.08	24.15		771	0.0	1392	7.38	7,980	0.3	0.3	461	385.8	70.5	7.88	*	1.7
5H-6, 135-150	42.95	7.19	23.23	24.88	770	0.4	1400	7.45	8,550	0.3	0.7	484	409.0	172.0	6.95		
6H-1, 135-150	44.95	6.99	21.65	23.22	797	0.0	1415	8.67	8,880	0.3	0.1	503	436.4	138.4	6.91	1.8	2.2
6H-2, 135-150	46.45			23.13	804	0.0	1474		9,340	1.5	1.5	525	461.9	124.9	3.86		
6H-4, 135-150	49.45	6.96	22.60	23.77	790	0.4	1432	9.25	8,730	0.4	1.2	504	428.6	148.9	6.13	1.1	1.1
7H-1, 135-150	54.45	7.13	16.32	18.15	848	0.0	1041	4.68	10,310	1.5	0.5	585	555.9	134.2	1.88	3.1	2.2
7H-2, 135-150	55.95	6.79	18.88	20.48	868	0.0	1119			5.3	1.1	594	551.9	139.1	4.23	3.9	2.6
9H-1, 135-150	73.45	6.76	17.39	21.24	937	0.5	940		14,050	1.0	0.5	728	746.8	182.8	3.64	3.4	2.6
9H-3, 135-150	76.45	6.61	18.04	22.84	947	0.0	923	5.11		0.6	0.3	722	767.5	195.2	2.41	3.1	1.8
10H-2, 135-150	84.45	6.61	17.07	21.63	935	0.0	879	4.70	15,460	1.5	0.5	773	856.5	218.9	3.18	2.5	1.3
10H-4, 135-150	87.45	6.61	17.09	21.27	980	0.0	922		15,860	1.4	0.4	793	865.3	223.1	2.58	3.1	1.7
11H-1, 135-150	92.45	6.71	16.20	18.63	1001	0.0			15,690	0.7	0.4	819	906.5	244.2	2.76	2.1	1.1
11H-2, 135-150	93.95	6.67	15.32	19.42	1000	0.0	911		15,820	0.8	0.5	809	912.0	239.6	2.43	3.1	1.0
12H-2, 135-150	103.45	6.66	16.18	20.38	1042	0.0	847	4.97	16,640	5.0	0.5	872	995.7	271.7	1.94	3.7	1.5
12H-4, 135-150	106.45	6.67	14.88	17.58		0.0		5.31	15,150	3.7	0.6	886	1026.7	281.7		6.0	2.5
13H-1, 135-150	111.45	6.65	15.25	19.28	1031	0.3	947		18,310	3.7	0.7	900	1066.0	288.0	1.25	4.6	2.2
13H-4, 135-150	115.95	6.44	16.55	21.17	1084	0.0			19,600	1.2	0.7	916	1083.6	300.2	1.37	5.2	2.2
14H-1, 135-150	120.95	6.50	15.57	23.28	1089	0.0	1070		19,280	9.4	1.0	964	1174.8	320.5	0.80	3.5	1.5
17H-1, 85-100	132.95	6.54	16.69	20.31	1135	0.3	847	3.99	21,710	15.1	2.0	969	1211.8	331.6	0.20	3.8	2.8
18H-2, 135-150	144.30	6.49	16.28	22.61	1170	0.2		3.17		29.5	2.0	1013	1450.1	338.1	0.58	4.1	2.3
18H-3, 0-20	144.45	6.55	14.42	18.47	1178	0.0		2.77	22,510	16.1	2.1	1025	1435.3	346.1	0.00	3.7	2.4
201-1227D-																	
1H-1, 0-1	0.00	7.37	3.30	3.23	556	28.7			0	2.2	0.1	92	27.4	0.5	0.00	0.4	0.3
1H-1, 0-15	0.00	7.59	3.60	3.83			535	2.34	0	2.5	0.1	91	27.8	0.3	0.12		
1H-1, 60-75	0.60	7.54	5.36	5.32	550	27.7	634	8.29	720	1.2	0.1	94	30.9	0.5	0.00	1.0	0.9
1H-1, 100-115	1.00	7.53	6.31	6.26	552	25.5	801	7.94	590	0.6	0.1	96	31.5	0.3	0.73		
1H-2, 30-45	2.09	7.50	7.90	7.87	557	24.1	875	8.03	860	0.5	0.1	95	34.9	0.6	1.21	1.4	1.3

Table T2 (continued).

Core, section, interval (cm)	Depth (mbsf)	pH	Alk (mM)	DIC (mM)	Cl ⁻ (mM)	SO ₄ ²⁻ (mM)	H ₄ SiO ₄ (μM)	PO ₄ ³⁻ (μM)	NH ₄ ⁺ (μM)	Fe (μM)	Mn (μM)	Sr (μM)	Li (μM)	Ba (μM)	ΣH ₂ S (mM)	Acetate (μM)	Formate (μM)
4H-1, 135-45	27.85	7.08	22.56	22.68	682	3.0	811	2.32	7,310	0.8	0.1	314	275.6	1.5			
4H-2, 135-150	29.35	6.89	20.91	21.20	704	2.7	987		6,930	0.5	0.1	335	276.9	1.6	7.16	1.2	0.6
4H-3, 135-150	30.85	7.07	20.81	22.58	706	2.6	935	3.00	7,040	0.2	0.1	343	290.0	2.0	6.71	1.3	1.3
4H-4, 135-150	32.35	6.94	21.69	23.13	700	2.5	1011		6,980	0.7	0.0	345	307.1	1.7	7.68		
4H-5, 135-150	33.85	6.87	22.07	24.05	714	2.6	1342	2.32	9,050	0.4	0.1	340	276.0	1.7	7.23	1.3	1.0
4H-6, 135-150	35.35	6.95	21.26	23.28			968	2.78	7,750	0.3	0.0	330	286.9	1.7	6.87	0.8	0.2
5H-1, 135-150	37.35	7.00	23.13	24.87	743	1.2	1089	10.23	8,030	0.9	0.0	409	371.5	3.7	8.70	*	1.2
5H-2, 135-150	38.85	6.84	23.06	24.91	746	0.9	1086	3.07	8,070	0.2	0.0	431	374.7	6.0	9.08	1.3	1.4
5H-3, 135-150	40.35	6.92	22.95	24.83	749	0.6	1174	4.15	8,580	0.5	0.0	446	395.4	11.0	8.43		
5H-4, 135-150	41.85	7.01	23.88	25.78	759	0.3	1305	5.04	8,410	1.7	0.3	464	404.5	34.0	7.95	1.4	1.1
5H-5, 91-106	42.91	7.04	22.65	25.17	763	0.0	1211	5.59	8,320	0.6	0.0	488	434.0	101.7	7.32	1.3	1.5
6H-2, 0-20	47.00	6.94	21.93	24.20	782	0.0	1467	9.40	10,150	0.4	0.2	515	476.6	112.0	7.53		
8H-2, 109-124	65.93	6.75	18.16	22.91	884	0.0	829		13,260	0.5	0.1	661	686.6	155.7	5.67	1.9	0.4

Note: Alk = alkalinity, DIC = dissolved organic carbon. * = coeluted with large lactate peak. This table is also available in [ASCII](#).

Table T3. Hydrocarbon gas concentrations in headspace, Holes 1227A and 1227D.

Core, section, interval (cm)	Depth (mbsf)	Methane (ppm in headspace)		Methane (μ M)	Ethane (ppm in headspace)		Ethane (μ M)	Propane (ppm in headspace)		Propane (μ M)
		20 min @ 60°C	24 hr @ 22°C		20 min @ 60°C	24 hr @ 22°C		20 min @ 60°C	24 hr @ 22°C	
201-1227A-										
1H-1, 130-135	1.30		37.8	7.5		0.2	0.03		0.0	0.00
1H-2, 130-135	2.80		37.7	7.0		0.2	0.04		0.0	0.00
1H-3, 130-135	4.30	14.9		*	0.0		*	0.0		*
1H-4, 0-5	4.50		55.8	11.1		0.3	0.06		0.0	0.00
2H-1, 130-135	6.90		31.9	7.9		0.5	0.12		0.0	0.00
2H-3, 130-135	9.90	11.2		*	0.0		*	0.0		*
2H-4, 130-135	11.40		66.8	14.7		1.5	0.32		0.0	0.00
2H-6, 130-135	14.40	51.3		*	0.7		*	0.0		*
3H-1, 130-135	16.40		145.1	29.4		2.5	0.50		0.0	0.00
3H-3, 130-135	19.40	93.1		*	1.3		*	0.0		*
3H-4, 130-135	20.90		167.2	35.9		2.6	0.55		0.0	0.00
3H-6, 130-135	23.90	108.8		*	1.8		*	0.0		*
4H-1, 97-102	25.57		166.7	35.1		3.5	0.73		0.0	0.00
4H-5, 90-95	31.16	115.1		*	2.1		*	0.0		*
4H-6, 145-150	32.81		162.5	33.3		2.9	0.59		0.0	0.00
4H-6, 145-150	32.81	213.4		*	4.3		*	0.0		*
5H-1, 130-135	35.40		282.5	55.3		3.4	0.67		0.0	0.00
5H-2, 130-135	36.90	471.8		*	3.6		*	0.0		*
5H-3, 130-135	38.40		1,014.9	209.2		5.8	1.19		0.3	0.05
5H-4, 130-135	39.90		1,564.5	322.9		9.0	1.86		0.6	0.12
5H-5, 130-135	41.40	1,638.1		*	5.5		*	0.4		*
5H-6, 130-135	42.90		2,354.1	570.6		8.5	2.05		0.9	0.21
6H-1, 130-135	44.90		3,286.5	972.2		7.1	2.10		0.8	0.22
6H-2, 130-135	46.40	3,319.9		*	5.0		*	0.7		*
6H-3, 130-135	47.90		6,594.5	2,052.4		9.8	3.04		1.7	0.53
6H-4, 130-135	49.40	1,922.1		*	3.2		*	0.4		*
7H-1, 130-135	54.40	6,878.3		*	6.8		*	1.4		*
7H-3, 0-5	56.10		14,174.6	2,592.1		12.6	2.31		3.5	0.64
9H-1, 130-135	73.40		7,201.9	1,306.6		8.0	1.45		3.1	0.55
9H-2, 145-150	75.05	5,350.7		*	6.1		*	2.3		*
9H-4, 0-5	76.60		6,590.2	1,307.4		8.3	1.65		2.7	0.54
10H-1, 145-150	83.05		16,620.1	3,226.4		11.0	2.14		3.7	0.72
10H-3, 145-150	86.05		16,718.0	3,377.5		13.3	2.68		4.4	0.90
10H-4, 130-135	87.40	8,497.2		*	8.4		*	2.4		*
11H-1, 130-135	92.40		9,972.4	1,940.1		8.8	1.71		2.7	0.52
11H-3, 0-5	94.10	6,534.5		*	7.5		*	2.6		*
12H-1, 145-150	102.05		5,836.4	1,017.0		3.9	0.68		0.8	0.14
12H-3, 145-150	105.05	2,051.9		*	3.7		*	1.8		*
12H-4, 130-135	106.40		7,211.5	1,291.3		7.4	1.32		2.3	0.42
13H-1, 130-135	111.40		13,908.4	2,486.6		11.7	2.09		3.1	0.56
13H-2, 145-150	113.05	10,091.2		*	8.9		*	3.1		*
13H-5, 0-5	116.10		15,127.4	2,778.2		9.7	1.79		2.7	0.50
14H-1, 130-135	120.90		14,111.4	2,591.6		10.9	2.00		2.6	0.47
14H-2, 145-150	122.55	3,157.0		*	2.6		*	0.8		*
14H-3, 0-5	122.60		8,125.0	1,454.9		9.5	1.70		3.5	0.63
17H-1, 80-85	132.90	1,908.5		*	5.3		*	2.3		*
18H-2, 0-5	142.95	4,296.6		*	9.9		*	2.7		*
201-1227D-										
1H-1, 30-35	0.30		16.8			0.0	0.00		0.0	0.00
4H-1, 130-135	27.80		174.2			3.6	0.62		0.0	0.00
4H-2, 145-150	29.45		210.1			4.9	0.84		0.0	0.00
4H-3, 130-135	30.80		190.1			3.9	0.71		0.0	0.00
4H-4, 145-150	32.45		150.8			3.3	0.63		0.0	0.00
4H-5, 130-135	33.80		165.9			3.8	0.70		0.0	0.00
5H-1, 130-135	37.30		782.6			5.2	0.99		0.2	0.05
5H-2, 130-135	38.80		1,378.9			7.5	1.58		0.7	0.14
5H-3, 130-135	40.30		1,754.5			8.3	1.82		0.4	0.09
5H-4, 130-135	41.80		1,698.7			6.8	1.76		0.6	0.14
6H-1, 145-150	46.95		2,829.5			4.0	1.09		0.7	0.18
6H-2, 145-150	48.45		2,037.1			3.2	0.84		0.1	0.03
8H-2, 104-109	65.88		16,087.7			12.1	2.38		3.0	0.58

Notes: * = not reported due to systematically lower yields compared to 24-hr extraction protocol. This table is also available in [ASCII](#).

Table T4. Calculated interstitial water hydrogen in incubated samples, Holes 1227A and 1227D.

Core, section, interval (cm)	Depth (mbsf)	H ₂ (nM)	Incubation temperature (°C)
201-1227A-			
2H-5, 55-61	12.53	0.32	11
3H-2, 65-71	17.25	0.38	11
3H-5, 91-97	22.01	0.25	11
5H-3, 55-61	37.65	0.27	11
5H-4, 130-135	39.90	0.28	11
5H-5, 86-92	40.96	0.42	11
6H-2, 60-66	45.70	0.29	11
7H-2, 74-80	55.34	0.35	11
9H-3, 65-71	75.75	0.25	11
10H-2, 50-56	83.60	0.27	11
11H-2, 88-94	93.48	1.18	11
12H-2, 83-89	102.93	0.48	11
13H-3, 60-66	113.70	1.09	11
14H-2, 80-86	121.90	0.49	11
18H-2, 102-108	143.97	0.39	11
201-1227D-			
1H-1, 153-159	1.53	0.95	11
1H-2, 50-56	2.29	0.40	11
1H-3, 60-66	3.89	0.56	11
4H-4, 70-76	31.70	0.41	11
4H-6, 108-114	35.10	0.39	11

Note: This table is also available in [ASCII](#).

Table T5. Potential contamination based on PFT and parallel bead counts, Holes 1227A and 1227D.

Core, section	Sample details	ng PFT/ g sediment	Potential μ L seawater/ g sediment	Beads counted	Beads/g
201-1227A-					
2H-2	Center	0.02	0.02		
2H-2	Outside	1.37	1.37		
2H-5	Center	0.02	0.02		
2H-5	Outside	0.13	0.13	3 in 50 fields	76
3H-5	Center	0.02	0.02		
3H-5	Outside	0.13	0.13		
5H-3	Center	BD	BD		
5H-3	Outside	1.46	1.46		
7H-2	Center	BD	BD	0	0
7H-2	Outside	6.39	6.39	0	0
12H-2	Center	0.05	0.05	1 in 53 fields	(16)
12H-2	Outside	0.86	0.86	8 in 50 fields	533
14H-2	Center	0.05	0.05		
14H-2	Center replicate	0.05	0.05		
18H-2	HTEW	0.08	0.08		
201-1227D-					
1H-3	Center	0.02	0.02	0	0
1H-3	Outside	0.55	0.55		
4H-6	Center	BD	BD		
4H-6	Outside	3.32	3.32		
4H-6	Center II	BD	BD		

Notes: Detection limit = 0.01 mL seawater/g sediment. PFT = perfluorocarbon tracer. BD = below detection. The potential for microbial contamination is based on 5×10^8 cells/L surface seawater. This may be viewed as an upper limit for microbial contamination because it requires that the sediment be porous enough to allow all of the contaminating cells to travel with the PFT. HTEW = high-temperature enrichment sample. The number in parentheses represents results based on a single, non-reproducible bead observation.

Table T6. Potential contamination of slurries based on PFT, Holes 1227A and 1227D.

Core, section	ng PFT/ mL slurry	Potential μ L seawater/ mL slurry
201-1227A-		
2H	BD	BD
3H	0.03	0.03
5H	BD	BD
7H	BD	BD
12H	BD	BD
201-1227D-		
4H	BD	BD

Notes: Detection limit = 0.025 μ L seawater/mL slurry. PFT = perfluorocarbon tracer. BD = below detection.

Table T7. Media inoculated with sample material from different depths, Holes 1227A and 1227D.

Hole:	201-1227A-						201-1227D-	
	2H 12	3H 21	5H 40	7H 55	12H 102	18X 144	1H 1	4H 34
Core:								
Depth (mbsf):								
Medium:								
Sed	15°C: MPN				15°C: MPN		15°C: MPN	15°C: MPN
Mono	15°C: MPN	15°C: EN	15°C: EN	15°C: EN	15°C: MPN		15°C: MPN	15°C: MPN
Ti-Mono	15°C: MPN	15°C: EN	15°C: EN	15°C: EN	15°C: MPN		15°C: MPN	15°C: MPN
Fe-Mono		15°C: EN	15°C: EN	15°C: EN				
Poly	15°C: MPN	15°C: EN	15°C: EN	15°C: EN	15°C: MPN		15°C: MPN	15°C: MPN
Ti-Poly	15°C: MPN	15°C: EN	15°C: EN	15°C: EN	15°C: MPN		15°C: MPN	15°C: MPN
Fe-Poly		15°C: EN	15°C: EN	15°C: EN				
Aro	15°C: MPN				15°C: MPN	15°C: MPN	15°C: MPN	15°C: MPN
Lac	15°C: MPN				15°C: MPN		15°C: MPN	15°C: MPN
Rad	15°C: MPN				15°C: MPN		15°C: MPN	15°C: MPN
Rad-Lac	15°C: MPN				15°C: MPN		15°C: MPN	15°C: MPN
Grad		15°C: EN	15°C: EN		15°C: EN		15°C: EN	15°C: EN
FERM-Glyc: 8.0	60°C: EN*				60°C: EN	60°C: EN	60°C: EN	60°C: EN
FERM-Glyc: 8.8	60°C: EN				60°C: EN			
FERM-Xyl: 8.0	60°C: EN*				60°C: EN	60°C: EN	60°C: EN	60°C: EN
FERM-Xyl: 8.8	60°C: EN				60°C: EN			
SRB: 8.0	60°C: EN				60°C: EN	60°C: EN	60°C: EN	60°C: EN
SRB: 8.6	60°C: EN				60°C: EN			
SRB benz: 8.0	60°C: EN				60°C: EN	60°C: EN	60°C: EN	60°C: EN
H ₂ /HCO ₃ ⁻ /FeIII: 7.9	60°C: EN				60°C: EN	60°C: EN*	60°C: EN	60°C: EN
H ₂ /HCO ₃ ⁻ /FeIII: 8.5	60°C: EN				60°C: EN	60°C: EN*	60°C: EN	60°C: EN
H ₂ /HCO ₃ ⁻ /MnIV: 7.8	60°C: EN				60°C: EN	60°C: EN*	60°C: EN	60°C: EN
H ₂ /HCO ₃ ⁻ : 7.8	60°C: EN				60°C: EN*	60°C: EN	60°C: EN	60°C: EN
H ₂ /HCO ₃ ⁻ : 8.8					60°C: EN			
C-18-lipo: 7.8	60°C: EN				60°C: EN	60°C: EN	60°C: EW	60°C: EN
C-18-lipo: 9.0					60°C: EN	60°C: EN*	60°C: EN	
Chlor: 7.8					60°C: EN	60°C: EN	60°C: EN	
201-1	RT, 50°C, 80°C: EN		RT, 50°C, 80°C: EN	RT, 50°C, 80°C: EN				
201-2	RT, 50°C, 80°C: EN							
201-3	RT, 50°C, 80°C: EN							
201-4	RT, 50°C, 80°C: EN							
201-5	RT, 50°C, 80°C: EN							
201-6	RT, 50°C, 80°C: EN	RT, 50°C: EN	RT, 50°C: EN	RT, 50°C: EN	RT, 50°C: EN			
201-7	RT, 50°C, 80°C: EN	RT, 50°C: EN	RT, 50°C: EN	RT, 50°C: EN	RT, 50°C: EN			
201-8	RT, 50°C, 80°C: EN							
201-9	RT, 50°C: EN	RT: EN	RT, 50°C: EN	RT: EN	RT, 50°C: EN			
201-10	RT, 50°C: EN	RT: EN	RT, 50°C: EN	RT: EN	RT, 50°C: EN			
201-11	RT: EN							
Fe(III)red	10°C: EN		10°C: EN		10°C: EN		10°C: EN	10°C: EN
Mn(IV)red	10°C: EN		10°C: EN		10°C: EN		10°C: EN	10°C: EN

Notes: Enrichment assays were qualitative (EN) or quantitative (MPN) and incubated at the temperature given and/or at room temperature (RT = 21°–25°C). * = enrichments were done in 150-mL serum bottles containing ~100 mL media and inoculated with 10 mL of core material. Other conditions are as given in “Microbiology,” p. 14, and Tables T4, p. 84, T5, p. 85, T7, p. 88, and media definitions are given in Table T9, p. 90, all in the “Explanatory Notes” chapter.

Table T8. Downhole temperature measurement summary, Hole 1227A.

Depth (mbsf)	Tool	Measurement location	Thermal conductivity (W/[m·K])	Temperature (°C)	Assessment
-10.0	WSTP	10 m above seafloor	—	8.9	
0.0	Adara	Seafloor; T Core 201-1227A-1H	—	8.6	
33.8	Adara	Core 112-684A-4H	—	10.4	
34.1	Adara	Core 201-1227A-4H	0.75	9.2	Too low
52.8	Adara	Core 112-684A-6H	—	11.1	
81.6	DVTP	B Core 201-1227A-9H	0.74	12.4	Short (~5 min)
110.1	DVTP	B Core 201-1227A-12H	0.76	<14.6	Very noisy
160.0	—	—	0.76*	16.4 [†]	

Notes: WSTP = Water Sampling Temperature Probe, DVTP = Davis-Villinger Temperature Probe. T = top of core, B = bottom of core. — = not applicable. * = average thermal conductivity. † = projected temperature at base of hole. The last line shows the temperature extrapolated to basement using linear fit in Figure F22, p. 54, and the mean thermal conductivity computed from data plotted in Figure F20A, p. 52.